Arab American University

Faculty of Graduate Studies

Investigation of the physical properties of $Tl_2InGaSe_4$ crystals

By

Tahani Mohammad Irshaid

Supervisor

Prof. Dr. Atef Fayez Qasrawi

This thesis was submitted in partial fulfillment of the

requirements for

The Master's degree in

Physics

February/2019

Investigation of the physical properties of $Tl_2InGaSe_4$ crystals

By

Tahani Mohammad Irshaid

This thesis was defended successfully on February 12th 2019 and approved by:

Committee members	Signature
1. Prof. Dr. Atef Fayez Qasrawi (Supervisor)	…….
2. Assoc. Prof. Dr.Hazem Khanfar (Internal examiner)	…….
3. Assoc. Prof. Dr. Khaled Ilaiwi (External examiner)	…….

Declaration

The work in this thesis, unless otherwise referenced, is the researcher's own work and has not been submitted elsewhere for any other degree or qualification.

Student's Name:

Signature:

Date:

Dedication

To My Parents

Acknowledgments

I praise God First and foremost. Starting with endless thanks for my mum and dad, thanks to my supervisor Prof. Dr. Atef Fayez Qasrawi. My genuine thanks to the members of Department of Physics at the Arab American University which granted the method to implementation this thesis, and gave me the possibilities of equipment's, tools and laboratories for continuous work to achievement my thesis. Special thanks go to Ms. Olfat Omareya who supported me through teaching the instrumentation and analysis. I would also like to thank all my friends and class members for the support during the thesis period.

Abstract

In this thesis, we have explored the physical properties of $Tl_2InGaSe_4$ single crystals, by means of structural, optical and electrical investigation. A layered nature of the crystal which shown in scanning electron microscope Contributed in nanotechnology application. The temperature dependent X-ray analysis in the temperature range of 300-470 K has shown that the crystals which exhibit both of the monoclinic and tetragonal phases have tendency to make the monoclinic structure more dominant of the tetragonal. The estimated grain size, microstrain, defect density and stacking faults are all observed to be sensitive to the temperature dependent structural modifications. Consistently the studies of the temperatures dependent energy band gap have shown that the energy bandgap linearly decreases with increasing temperatures. In addition, the illumination dependent current-voltage characteristics have shown that the crystals with high sensitivity and less dependence of barrier height on light intensity. Furthermore, the impedance spectroscopy analysis in the frequency domain of 10-1800 MHz, revealed possible tunability of the capacitance nominating the crystals for use as varicap devices.

List of content

List of table

List of figures

List of Symbols

Symbol	Acronym
C	Capacitance
L	Inductance
R	Resistance
Vs	Source voltage
V_c	Capacitor voltage
V_L	Inductor voltage
V_R	Resistor voltage
X_L	Inductive reactance
X_C	Capacitive reactance
Z	Impedances
I_S	Supply current
I_C	Capacitor current
I_L	Inductor current
I_R	Resistor current
d	Interplanar spacing
h,k,l	Millir indices
α,β,γ	Angles of the structure
t	Thickness
D	Crystalline size
ε	Strain
n	Ideality factor
SF	Structure Factor
R	Reflection
T	Transmittance
a	Absorption coefficient
ϕ_b	barrier height
h	Planck constant
E_g	Energy indirect bandgap
E_{gi}	Energy direct bandgap
I_d	Dark current
S	Sensitivity
A*	Richardson mechanism
K	Boltzmann's constant
λ	Wavelength
I_{ph}	Photocurrent
m*	effective mass

Chapter One
Introduction and Literature Survey

Thallium Indium Gallium Selenium ($Tl_2InGaSe_4$) single crystals are composed of the interaction $TlGaSe_2$ layered crystal and $TlInSe_2$ crystal chain. These crystal compounds attracted the attention of many scientists owing to it is usability in technological applications. Especially, applications which require high photosensitivity in the visible region of light spectrum, optical second-harmonic generation, and high birefringence along region of 0.5-14.0 μm. $TlInSe_2$ crystal is also reported to exhibit switching and memory effects [1,2]. For $Tl_2InGaSe_4$ crystal there are just few studies which concern the physical properties, including optical absorption spectra, temperature dependence of the band gap, Raman spectra and photoconductivity [3,4].

Ternary thallium chalcogenides presented by $TlInSe_2$ and $TlGaSe_2$ have been studied widely in last few years. These crystals are very substantial in view of their possible technological applications as optoelectronic devices and as a filter material for optical applications. This importance basically comes from their broad transparency rang and high photosensitivity. $TlGaSe_2$ has an elevated photosensitivity in the visible domain range of spectrum. High birefringence in coupling with a large sensitivity rang of 0.6-16 mm [3,5]. $TlGaSe_2$ compound is a monoclinic crystal structure with lattice parameters a= 10.879, b= 10.79, c= 15.707 Å and β= 100.47º, respectively. The unit cell consists of two layers rotated with each other by 90º. The ions of univalent thallium are situated in the trigonal voids between the GaSe complexes. Studies on the fundamental optical absorption in $TlGaSe_2$ crystal, where the fundamental absorption edge is formed by the direct and indirect transitions with room-temperature energies varying over large ranges: E_g = 2.08-2.23 eV and E_{ig} = 1.83-2.13 eV.

$TlInSe_2$ crystals belong to the group of semiconductor with the chain structure of crystal lattice and is analog of thallium selenide where trivalent Tl^{+3} ion are replaced with In^{+3} [2,3]. This crystal is composed of two dimensional alternating layers; each layer is rotated with connect to the previous layer by 90^o [3]. This crystal structure are negatively charged chains which placed along the tetragonal c-axis. The forces inside the chain have an ionic-covalent character while the forces between the chains are week of van der waals type. The chemical formula for $TlInSe_2$ may be written as $Tl^{+1}(In^{+3}Se_2^{-2})^{-1}$. It's easy to cleave the crystals along c-axis into two mutually perpendicular plane (100). $TlInSe_2$ has an indirect optical band gap of $E_g \approx 1.4eV$ at room-temperature and is considered to be a potential material for optoelectronics.

In optoelectronic lasers or LEDs, defects may insert nonradiative recombination centers to lower the internal quantum efficiency. In the case of electronic devices, defects introduce scattering centers lowering carrier mobility. Therefore, it salutary to get facts on the parameters of trapping centers in semiconductors to obtain high-quality devices. Among the various experimental methods to calculate the properties of thermally stimulated luminescence (TL) measurements, trap centers supply extensive information on trap states [3].

In this work, we investigate the properties of the $Tl_2InGaSe_4$ single crystals. Especially, physical nature of crystal, optical characteristics, electrical and impedance spectroscopy which will be explored by X-ray, EDX, UV-VIS, SEM, techniques, impedance spectroscopy and I-V characteristic, respectively. In this thesis, the second chapter will concentrate on some of the theoretical relations which are required for predicting the results from the experiments. The next chapter explains the experimental steps that are used to deal with the measurements.

This chapter also contain some of the schematic presentation of the measuring devices. The following chapter (chapter 4) detected the results that mentioned in details, some of the data which is subjected to computational analysis to obtain more information about $Tl_2InGaSe_4$ crystal. Finally, chapter 5 contain conclusion that is derived from previous results in chapter 4.

Chapter Two
Theoretical Background

In this chapter we review some important theoretical modules that are needed to explain the experimental observations. Some of the necessary derivations, will be carried out for the purpose of guiding the reader needs.

2.1: Scanning Electron Microscopy (SEM)

The scanning electron microscopy (SEM) technique is used to describe the surface morphology of deposited single crystals. This technique also includes a focused beam of electrons in order to scan the surface of the single crystal samples based the precept that secondary electrons will be created by inelastic collisions of energetic primary electrons. These electrons return from a sample ever after they are enticed to a grid under low potential and then accelerated due to a higher electron potential [2,6].

2.2: The X-ray diffraction

X-rays are a form of electromagnetic radiation, which have an energy ranging between 100 eV and 100 KV. In diffraction experiments a short wavelength X-rays only are used, which is in the range of 0.1 Å to a few angstroms. This reason helps us to investigate the structural arrangement of molecules and atoms of most of materials. The X-rays collide with electrons of atoms when they are sent to a material before deflected away [2,7].

The scattered X-rays have the same wavelength like that of incident, for the collisions between electrons and incident photons are elastic, the scattered X-rays that are measured in diffraction experiments carry information about the atomic distribution of materials. The incident X-rays are reflected on the array which interact with atoms the crystal as shown in Fig 2.1. This design represents Bragg's law. Mathematically, the Bragg's law is expressed by the equation [8,9],

$$n\lambda = 2d \sin\theta \qquad (2.1)$$

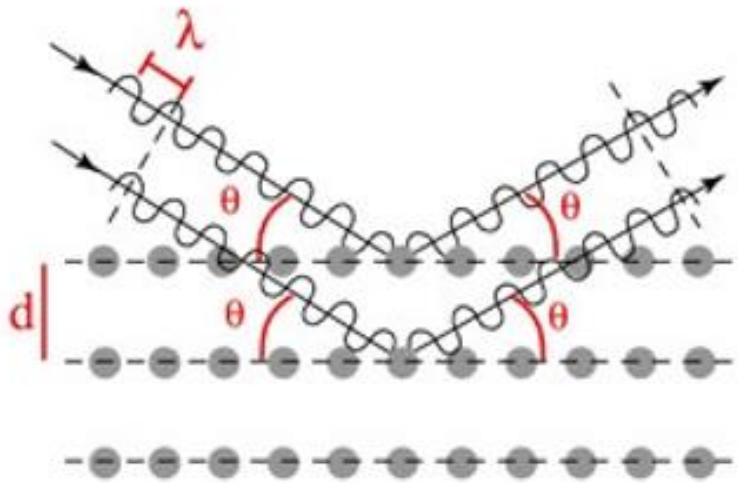

Fig. 2.1: Bragg's law in X-ray diffraction of a crystal lattice [3].

Where λ is the wavelength of the X-rays, n is an integer represents the order of reflection maximum, θ is the angle of reflection which is equals the angle of incidence, and d is the interplanar spacing between atomic planes. Interplanar spacing is defined as the spacing between planes in a crystal and is denoted as d_{hkl}, which can be expressed in most general form called triclinic structure by [3]:

$$\frac{1}{d_{hkl}^2} = 1/[1 + 2\cos(\alpha)(\alpha)\ \cos(\beta)\cos(\gamma) - (\cos)^2(\alpha) - (\cos)^2(\beta) - (\cos)^2(\gamma)]$$

$$\times [\frac{h^2\sin^2(\alpha)}{a^2} + \frac{K^2\sin^2(\beta)}{b^2} + \frac{l^2\sin^2(\gamma)}{c^2}$$

$$+ \frac{2hk}{ab}\big(\cos(\alpha)\cos(\beta) - \cos(\gamma)\big) + \frac{2kl}{bc}(\cos(\beta)\cos(\gamma) - \cos(\alpha))$$

$$+ \frac{2lh}{ac}(\cos(\gamma)\cos(\alpha) - \cos(\beta))] \qquad (2.2)$$

Where a, b and c are the lattice constants, α, β, and γ are the angles of the triclinic structure which is shown in Fig. 2.2 for the lattice structure and h, k, and l are the Miller indices.

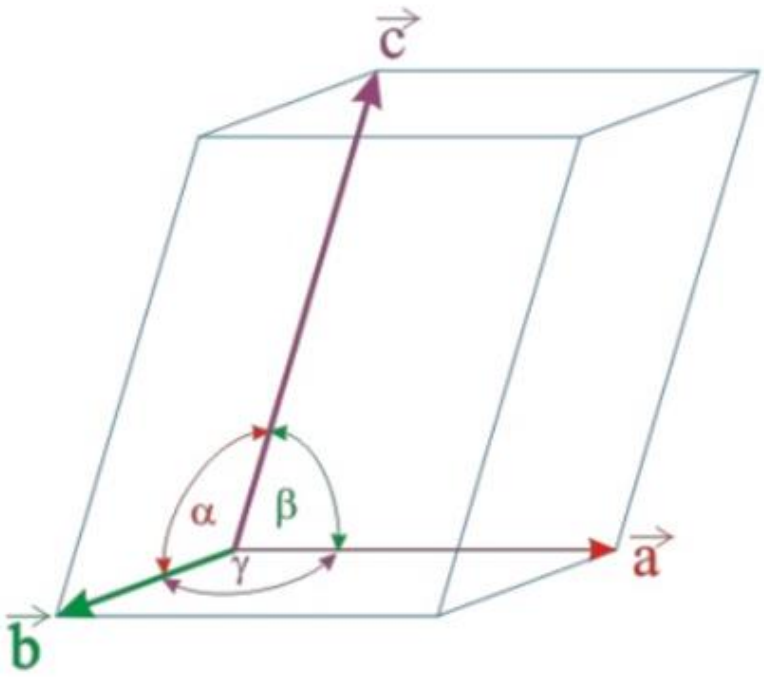

Fig. 2.2: The triclinic structure.

Equation (2.2) can be modified to reveal the other structural phases like cubic indicate

(1) monoclinic equation

a, b, c and $\alpha = \beta = \gamma = 90^{o}$, $\cos\alpha = \cos\gamma = 0$, $\sin\alpha = \sin\gamma = 1$

$$\frac{1}{d_{hkl}^2} = \frac{\frac{h^2}{a^2}+\frac{k^2}{b^2}\sin^2\beta+\frac{2hl}{ac}\cos\beta}{1-\cos^2\beta} \tag{2.3}$$

(2) Rhombohedral equation

$a = b = c$, $\alpha = \beta = \gamma \neq 90$

$$\frac{1}{d_{hkl}^2} = \frac{(l^2+k^2+h^2)\sin^2\alpha+2(hk+kl+hl)(\cos^2\alpha-\cos\alpha)}{a^2(1-\cos^2\alpha+2\cos^3\alpha)} \tag{2.4}$$

(3) Hexagonal equation

$a = b \neq c$, $\alpha = \beta = 90$, $\gamma = 120$

$\sin\alpha = \sin\beta = 1$, $\sin\gamma = 0.8$, $\cos\alpha = \cos\beta = 0$, $\cos\gamma = -\frac{1}{2}$

$$\frac{1}{d_{hkl}^2} = \frac{4}{3}\left(\frac{h^2+k^2+hk}{a^2}\right) + \frac{l^2}{c^2} \quad (2.5)$$

(4) Orthorhombic equation

$\cos\alpha = \cos\beta = \cos\gamma = 0, \sin\alpha = \sin\beta = \sin\gamma = 1$

$a \neq b \neq c, \alpha = \beta = \gamma = 90$

$$\frac{1}{d_{hkl}^2} = \frac{h^2}{a^2} + \frac{k^2}{b^2} + \frac{l^2}{c^2} \quad (2.6)$$

(5) Cubic equation

$a = b = c, \alpha = \beta = \gamma = 90$

$$\frac{1}{d_{hkl}^2} = \frac{h^2+k^2+l^2}{a^2} \quad (2.7)$$

(6) Tetragonal equation

$a = b \neq c, \alpha = \beta = \gamma = 90,$

$\cos\alpha = \cos\beta = \cos\gamma = 0, \sin\alpha = \sin\beta = \sin\gamma = 1$

$$\frac{1}{d_{hkl}^2} = \frac{h^2+k^2}{a^2} + \frac{l^2}{c^2} \quad (2.8)$$

The analysis of the X-ray broadening allows determining the crystal Structural parameters presented by crystal crystal size and the microstrain can be found by using scherrer equation (2.2) [9]. This equation is applicable to grains less than 0.2 μm.

2.2.1 Derivation of scherrer equation

Scherrer equation is a method which is used to calculate the microstrain (ε), stacking faults (SF) and crystallite size (D).

Bragg's law is the simplest way which is used to derivative the scherrer equation, by multiplying both side of equation (2.1) by an integer m, then [10,11] we have:

$$m\lambda = 2md\ sin\theta, \text{where n=1.} \quad (2.9)$$

In above equation m multiplied with interplanar (d) equal the thickness (t) of the crystal, then the equation (2.10) becomes:

$$\mathrm{m}\,\lambda = 2\,\mathrm{t}\,\sin\theta \quad (2.10)$$

By differentiating both side of equation, and m λ is constant, the equation simplifies as:

$$0 = 2\,\Delta\,\mathrm{t}\,\sin\theta + 2\,\mathrm{t}\cos\theta\,\Delta\theta \quad (2.11)$$

$$\mathrm{t} = \frac{\Delta\,\mathrm{t}\,\sin\theta}{\cos\theta\,\Delta\theta} \quad (2.12)$$

The small increment thickness is d, meanly ($\Delta\,\mathrm{t} = \mathrm{d}$), $\mathrm{d}\,\sin\theta = \lambda/2$, $\Delta\theta$ is the width of the peak and must be taken the absolute value to get $\Delta\theta$ positive value, mathematically ($2\,\Delta\,\theta = \beta$), this yield to:

$$t = \frac{\mathrm{d}\,\sin\theta}{\cos\theta\,\Delta\theta} = \frac{\lambda}{2\,\cos\theta\,\Delta\theta} \quad (2.13)$$

$$\mathrm{t} = \frac{\lambda}{\cos\theta\,\beta} = \mathrm{D}$$

We get some equation for strain, stacking faults and crystal size by using gassian function which is used to describe the peak, so

$$\varepsilon = \frac{\beta}{4tan\theta} \quad (2.14)$$

$$\mathrm{SF} = \frac{2\pi^2\,\beta}{45\,\sqrt{3}\,\tan\theta} \quad \text{and} \quad (2.15)$$

$$\mathrm{D} = \frac{0.94\,\lambda}{2\,\cos\theta\,\Delta\theta} \quad (2.16)$$

Where β is the full width at half maximum intensity of peak, crystallite structure is constant which equal 0.94, ε is strain and D is the average crystal size.

2.3: Optical properties

As we know, the light is an electromagnetic wave. When the beam of the light which has an intensity I_o hits the single crystal sample with d thickness, the photons will interact with the atoms, the beam wave is reflected (R). This reflected part of the original intensity, can be expressed in (1-R) from the original intensity.

The beam which propagates through the single crystal sample after it enters the material has an absorbed intensity multiplied by ($e^{-\alpha d}$) factor, where α in the factor the absorption coefficient. This coefficient can be used to calculate the energy band gap (E_g) of semiconductors, through Tauc's equation [12,13],

$$(h\nu)^p \alpha \left(E - E_g\right) \quad (2.17)$$

Where ($h\nu$) is photoenergy, p is constant, values of p are 1/2, 3/2, 2 and 3 which represent direct allowed, direct forbidden transition, indirect allowed and indirect forbidden transition respectively.

Transmission like reflection is depends on measuring the amount of light transmitted at specified wavelength. The processes after the light beam enter the material are divided into some reflected, some absorbed and some pass through the material [14],

The Transmission is given by:

$$T = (1 - R)^2 e^{-\alpha d} \quad (2.18)$$

$$\alpha = -\ln\left(\frac{T}{(1-R)^2}\right)/d$$

For cases where the crystal exhibit very low reflectivity the term R ignored and becomes:

$$\alpha = -\frac{1}{d}\ln\left(\frac{1}{T}\right) \quad (2.19)$$

Where transmission depends on the absorption coefficient.

2.4: The RLC circuit

The RLC circuit is composed of a capacitor C, inductor L and a resistor R. In Fig. (2.3) [15], the RLC circuit is in series connection in which the current is the same for each component and amplitude of the source voltage (V_s) is divided to three branch voltage V_C, V_L and V_R [15].

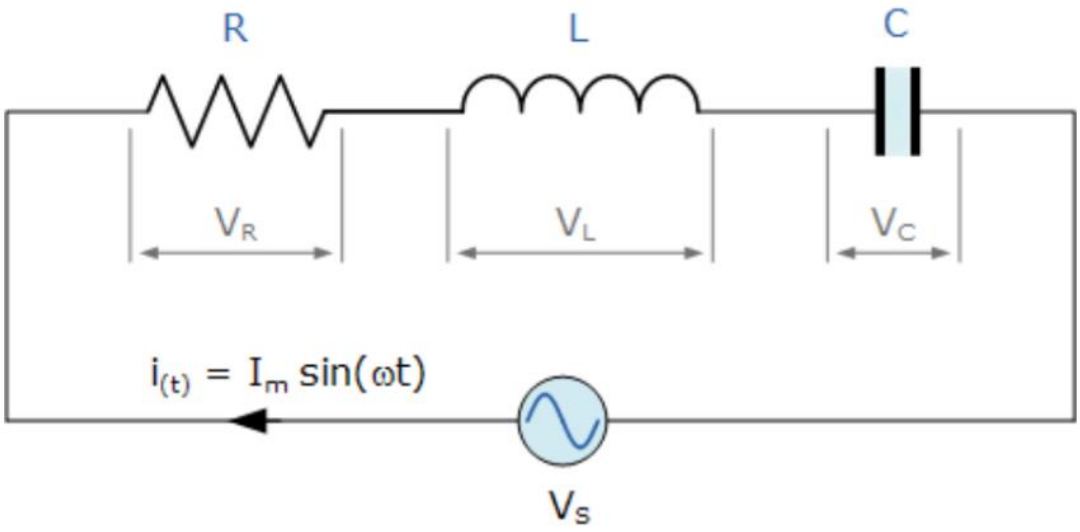

Fig. 2.3: The series RLC circuit.

The three component voltages are given by:

$V_c = I X_c$, $V_L = I X_L$ and $V_R = I R$

By applying Kirchhoff's voltage Law [6], to find Vs as the phasor sum of the component voltages.

$$Vs = V_R + V_L + V_C \tag{2.20}$$

When $X_L > X_C$, then the V_L=I X_L is greater than V_C=I X_C as a result the V_L and V_C are directed towards V_L. Current lead to (VL-VC) as a result the circuit reactance is called inductive.

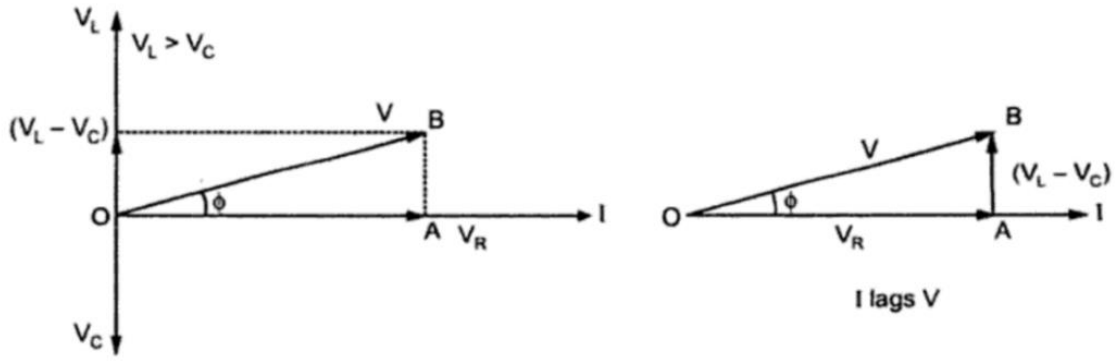

Fig.2.4: The phasor diagram and voltage triangle for $X_L > X_C$.

In the series RLC circuit, a phasor diagrams in Fig.2.4, the summation of V_R and (V_L-V_C) gives the source voltage is given by [17]:

$$Vs = \sqrt{V_R^2 + (V_L - V_C)^2}$$

$$= I\sqrt{R^2 + (X_L - X_C)^2}$$

$$= Z \qquad (2.21)$$

Where, in eq.2.6 and 2.7, X_L is the inductive reactance and X_C is the capacitive reactance. The impedance (Z) depends on inductive, resistive and capacitive reactance's of the circuit.

In the parallel RLC circuit as shown in Fig. 2.5, the supply current I_s α is the vector individual for three elements α I_C, I_L and I_R

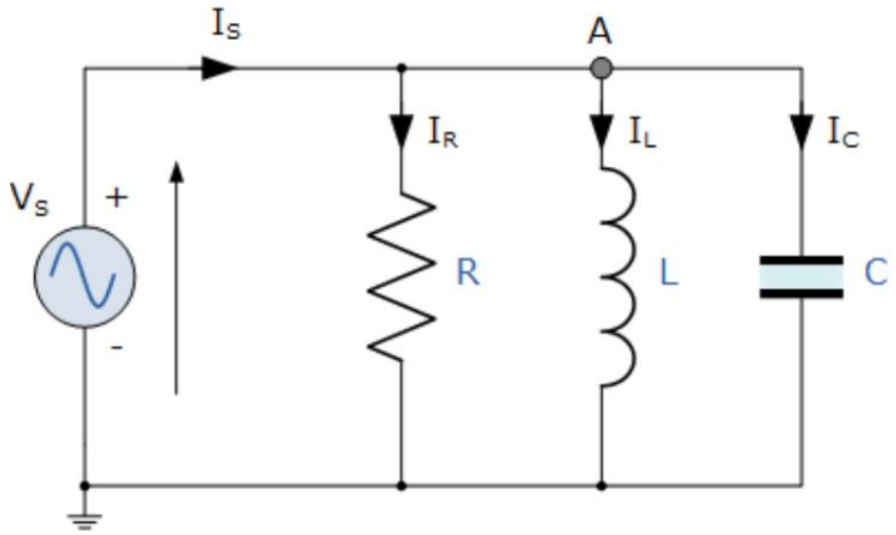

Fig. 2.5: The parallel LRC circuit.

The voltage drops across the circuit is the same foe all components which can be used as a reference vector to drown the currents vectors as a result the vector Is can calculated by added the I_L and I_C vectors and then the result is added to I_R vector.

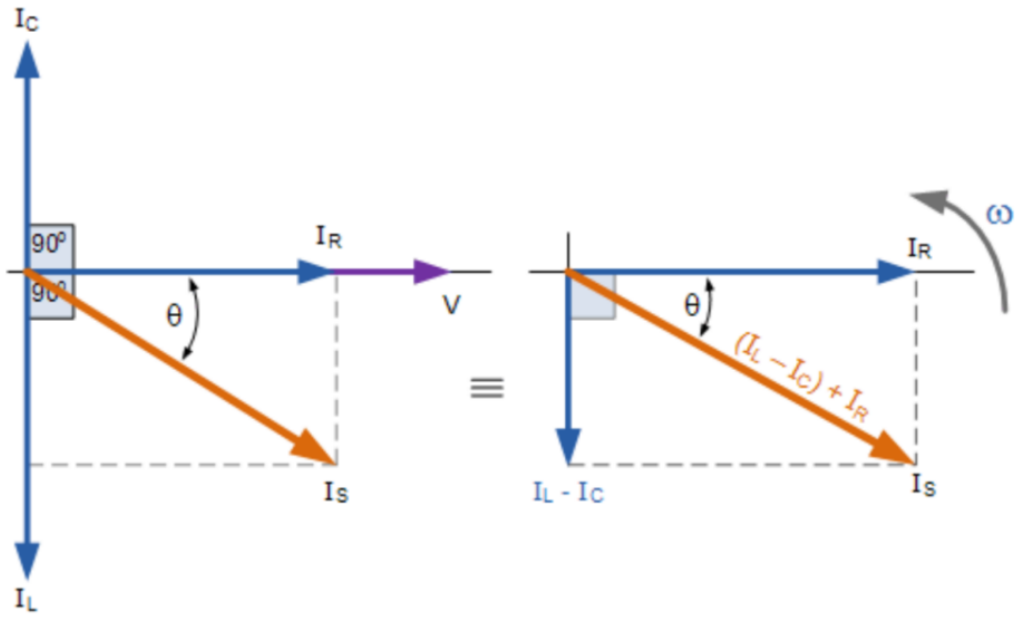

Fig.2.6: Phasor diagram for parallel RLC circuit.

By using Pythagoras's theorem, the magnitude of the branch currents at the X-axis and y-axis are calculated as a result, the total current Is can be found

$$I_s = \sqrt{I_R^2 + (I_L - I_C)^2},$$

Where $I_R = \frac{V}{R}$, $I_L = \frac{V}{X_L}$ and $I_C = \frac{V}{X_C}$

$$= \sqrt{(\frac{V}{R})^2 + (\frac{V}{X_L} - \frac{V}{X_C})^2} \quad (2.23)$$

The relation that represents the circuit impedance Z after combination of R, X_L and X_C is given by

$$z = \frac{1}{\sqrt{\left(\frac{1}{R}\right)^2 + \left(\frac{1}{X_L} - \frac{1}{X_C}\right)^2}} \quad (2.24)$$

2.5 Current transport processes

Majority carriers are expresses as the main reason for transporting the current in metal-semiconductor contacts. Under forward biasing conditions, there are five basic transport processes for this bias (1) holes injected from the metal which diffuse into the semiconductor, (2) recombination in the space – charge region, (3) diffusion of electrons in the depletion region, (4) quantum mechanical tunneling of electrons through the barrier, and (5) emission of electrons from the semiconductor over the potential barrier to the metal. High electric field at the metal-contact or interface current which may in leakage current [17,18].

2.5.1 The schottky diode

Schottky diode operates as a majority-carrier device with inherent fast response and it is some extent electrically such as a one-sided abrupt p-n junction. The terminal functions of a p-n junction diode can general be performed by a schottky diode with one exception as a charge-storage diode. This happens because a majority-carrier devices exhibit short charge-storage time. In schottky diode, the current density is larger due to the smaller

built-in potential as well as the nature of thermionic emission compared to diffusion [17,19].

2.5.2 Thermionic emission theory of diodes

The thermionic emission theory is related with a potential barrier ϕ_o and majority carrier current. The condition that must apply is the barrier height be much larger than KT. The mathematical relation which is expressed to the thermionic emission theory is given by Richardson equation [17,20]:

$$I = AA^{*}T^{2}\exp(\frac{-q\phi_b}{KT})(\exp(\frac{qV}{nKT}) - 1) \quad (2.25)$$

Derive Richardson equation we get:

$$\ln(I) = (\ln(AA^{*}T^{2}) - \frac{q\phi_b}{KT} - \frac{qV}{4KT} \quad (2.26)$$

Where A* is Richardson mechanism, n is ideality factor and A is the device area, T is device temperature and K is Boltzmann's constant and ϕ is the field-dependent activation energy that points a schottky-barrier height in the existence of the electric field.

2.5.3 Photoelectric measurement

The photoelectric measurement is a way of calculating the barrier height. Photocurrent may be generated, if a monochromatic light is fallen at metal surface. In the schottky-barrier diode, there are two kinds of carrier excitation can exist that share to Photocurrent, (1) band to band excitation, (2) excitation over the barrier which is only useful to measure the barrier height [17,21]. The metal film should be thin to let the light penetrate it.

2.5.4 Generation-Recombination process

In a semiconductor system, the thermal-equilibrium condition is disturbed (i.e., $pn = n_i^2$), where p and n are a hole carrier and electron carrier concentration respectively, $n_i^2$is intrinsic carrier concentration process exist to restore the system to equilibrium (i.e., $pn \neq n_i^2$) [17,22]. Where These processes are thermal generation when $pn < n_i^2$ and recombination when $pn > n_i^2$. Fig.2.7 represents the band-to-band electron-hole recombination. Radiative process occurs when the energy of an electron in transition from the conduction band to the valance band or by Auger process. Where this process transfer of the energy to another free electron or hole. The former process is the inverse of direct optical absorption.

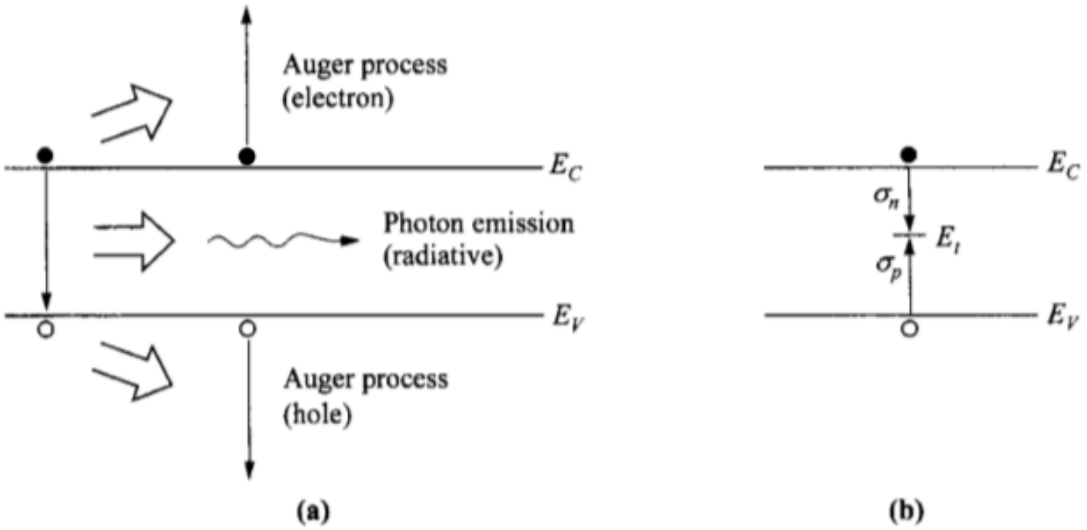

Fig.2.7: (a) Band-to-band recombination and (b) Recombination through nonradiative (single-level trapes) [17].

2.5.5 Definition of photosensitivity and photocurrent

Photosensitivity is the collection of specific sensitivity and device parameters known as photoconductivity gain, Specially the gain of a photodetector can be defined. Through the photo-thermoelectric effect, temperature gradients induced by non-uniform heating under

illumination can also generate a photovoltage or photocurrent which response to the incident light power [17,23].

Chapter Three
Experimental Details

3.1 Single Crystal Preparation

The crystals under study are prepared by Prof. N.M.Gasanly in Baku university. The Bridgman method is used to synthesize $Tl_2InGaSe_4$ single crystal with high purity elements (99.999%) from the stoichiometric melt of the crystal composers [24,25]. Materials are locked in evacuated (10^{-5} Torr) slica tubes with a tip at the bottom. The ampoule is transferred in a perpendicular oven through a thermal gradient of 30^{o} C cm^{-1} at a rate of 1.0 mm h^{-1}as shown in Fig.3.1.

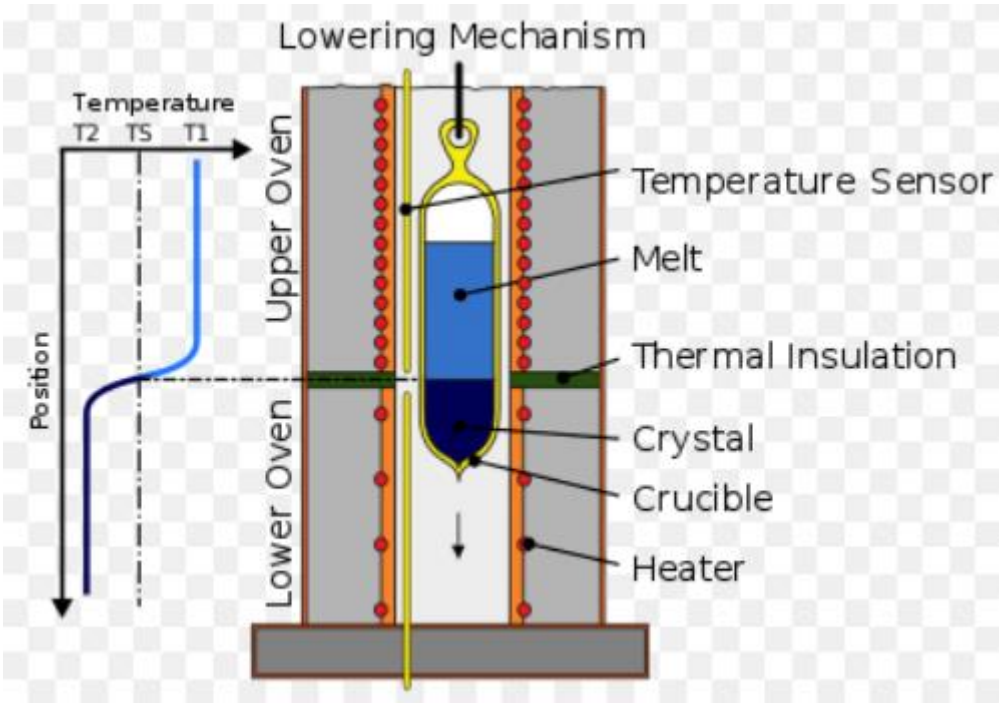

Fig. 3.1: The Bridgman method mechanism.

3.2 Scanning Electron Microscopy (SEM) measurement

The layers of the crystal are monitored by using COXEM-200 scanning electron microscope. The microscope is shown in Fig.3.2 which available at physics lab. The SEM images were also recorded at different exciting voltages in the range of 15-30 KV in Fig. (4.1-4.3). The measured crystals were coated with gold using ion coater (Fig.3.2(b)). The thickness of the gold layer was 10 nm.

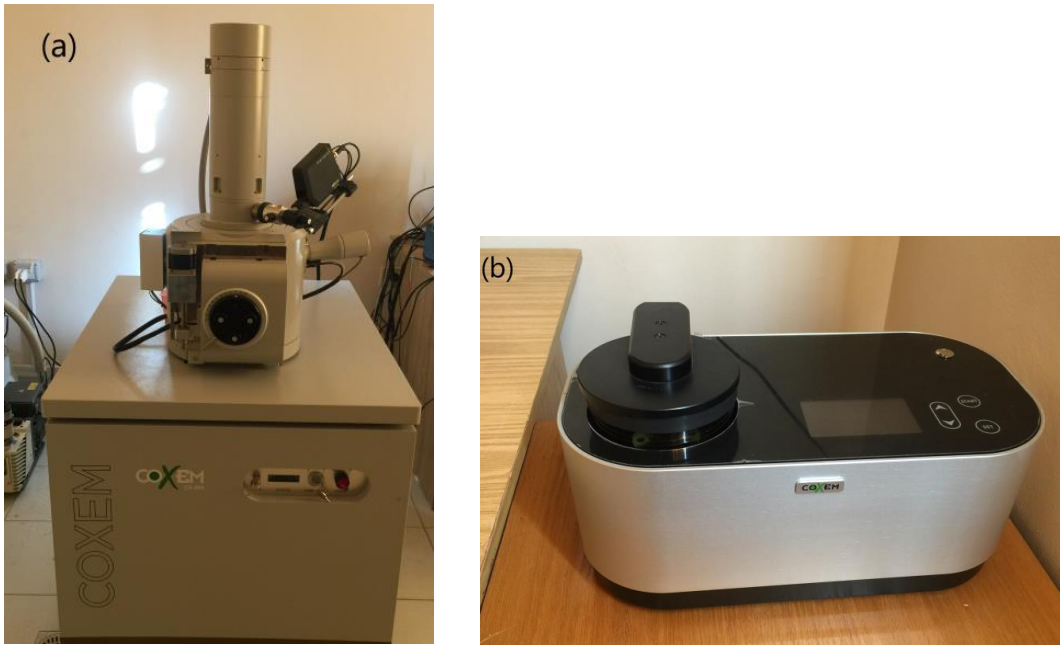

Fig.3.2: (a) Scanning Electron Microscopy (SEM) COXEM-200, (b) coater.

3.3 The X-ray diffraction (XRD) measurements

X-ray diffraction experiments are used to study the structural parameters of samples. In this experiment, a Rigaku Miniflex 600 diffractometer with Ka radiation of a copper anode is used. The X-ray beamcurrent is 15 mA with applied voltage of 40 KV and average wavelength of 1.5405 Å were used to determine the lattice structure of $Tl_2InGaSe_4$ single crystals. The diffraction angle was varied in the range of 10-70 °. The

analysis was carried out by “Treor-92” software package which is available in our Lab. Fig.3.3 represents X-ray diffraction schematics. The detector measures the intensity with enumerated angle 2θ and the single crystal sample moves by θ. Slit width of 1.0 mm is used in order to regulate the size and form of the beam of the X-ray. The scan rate was 2^{o}/min and the 2θ step size was 0.05^{o} [3,26].

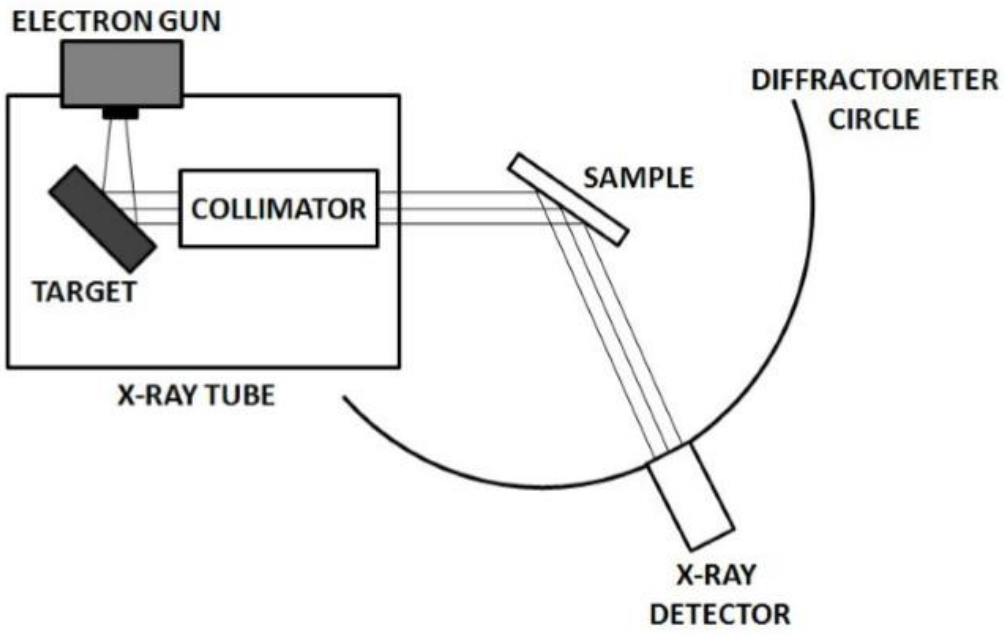

Fig. 3.3: Schematic of X- ray diffraction [3].

3.4 “Hot-Probe” Technique

Fig.3.4 shows the “Hot-Probe” Technique which was used to distinguish between p and n-type conductivity for $Tl_2InGaSe_4$ single crystal semiconductor which was n-type. This technique uses standard digital multimeter (DMM) and a heater. The cold iron is attached to the negative terminal of the multimeter, while the hot one is connected to the positive terminal. When the probes are applied to the sample and the DMM is reading a negative voltage, the probes indicating p-type materials. In contrast, positive voltages indicating

the n-type materials. The reason for this is the holes in p-type and electrons in n-type which are carriers that move in the semiconductor. From the hot probe to the cold probe. An increase in the number of higher energy carries is created due to the heat from the probe [15].

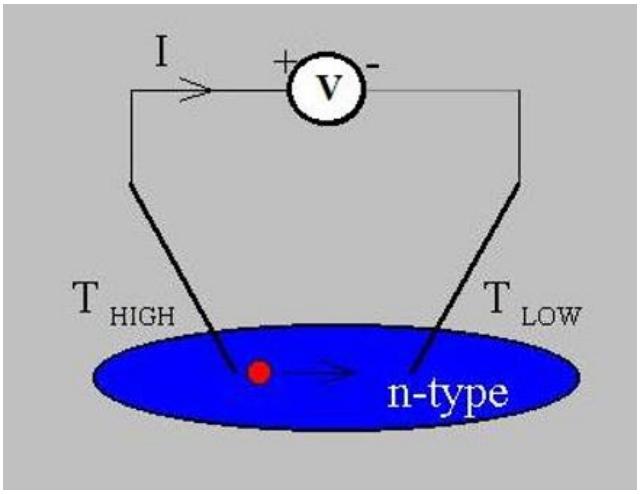

Fig. 3.4: Experimental set-up of the “hot-probe” experiment for n-type material [15].

3.5 Optical measurements

A thermo-scientific evolution 300 spectrophotometer is employed to measure the optical reflectance and transmittance with temperature in the incident light wavelength range of 300-1100 nm. The system is shown in Fig. 3.5. Both of the transmittance and reflectance are measured at normal incidence. The optical band gap, interband transition, materials absorbability and dielectric spectra are determined from the transmittance T% and reflectance R% measurement.

Fig. 3.5: The UV-VIS spectrophotometer.

3.6 Current-voltage measurements

By using Keithley programmable 230 voltage source and Keithly 480 picoammeter which the electrical conductivity and temperature dependent current-voltage characteristic. The data were transported using Keithley high-quality low-noise.

1) Put electrical contacts points silver and carbon on the $Tl_2InGaSe_4$ single crystal sample.
2) By using a bar copper metal which surrounded by copper-nickel wire which has low resistivity work as heater for the single crystal.

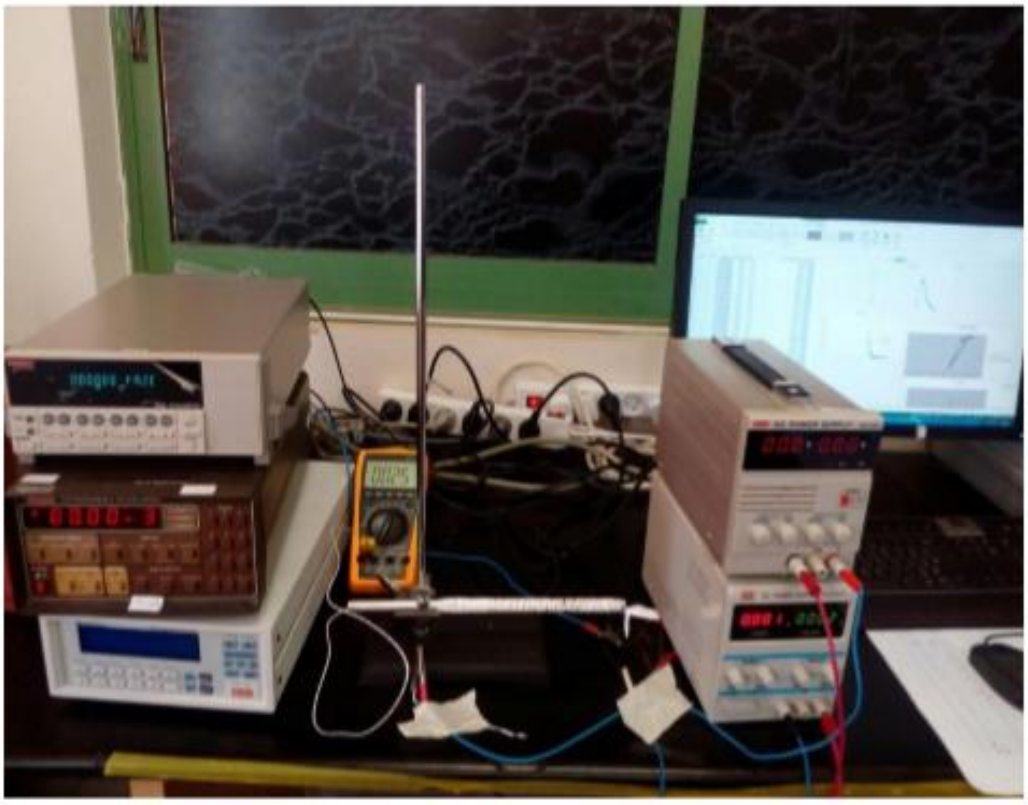

Fig. 3.6: Setup of (I-V) characteristic with temperature dependent of electrical conductivity.

3.7 Impedance measurements

Agilent 4291BRF single Generator impedance analyzer (10MHz-1.8GHz) is used for providing the AC signal. The total impedance (Z) which is composed of reactive parts and resistive parts, capacitance (C) and inductance (L) are measured by the instrument which is shown in Fig. 3.7. The signal power was registered with the assist of MATLAB software. As an experimental condition, we restricted the signal to have a voltage of 0.1 V and the frequency was changed in the range of 10-1800 MHz.

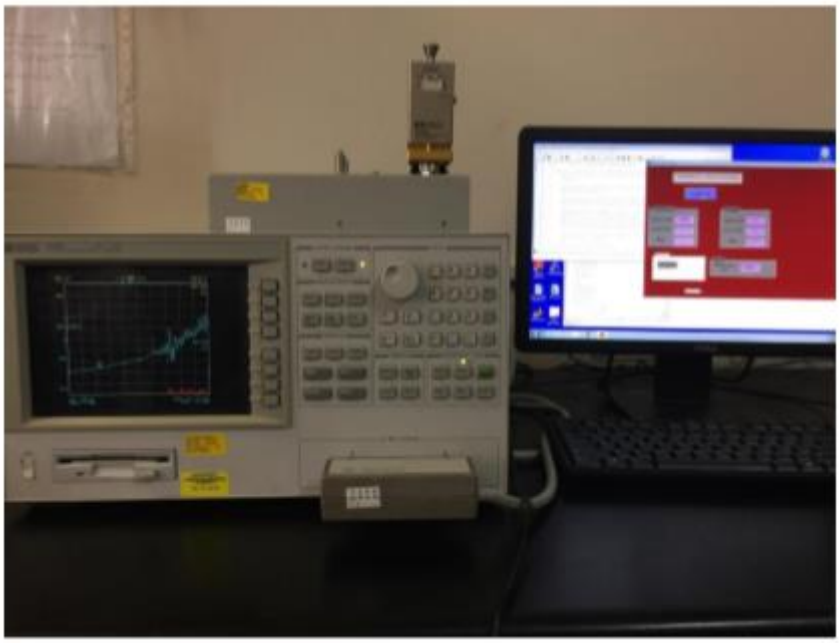

Fig. 3.7: Setup for the impedance measurements.

Chapter Four
Results and Discussion

4.1 Scanning electron microscopy analysis

The optical image for the $Tl_2InGaSe_4$ single crystals is shown in Fig. 4.1. The obtained crystal parts are dark red colored. To investigate the nature of these crystals. The crystal was broken and coated with Au layer of 10 nm then inserted into scanning electron microscope [27]. The image for the crystals which is shown in Fig 4.1, indicate a layered nature of the crystal. The very dense layers are easily distinguishable from each other. Most of the layers exhibit the same shape with almost no irregular appearance between the layers. As appears in Fig. 4. 2, when the electron beam voltage is raised top 30 KV and the layers are viewed with larger magnification (10000 times), one may observe exactly parallel nanosheets being stacked on each other's. All the sheets exhibit the same thickness. Even for large crystal parts that could be as long as 0.2 cm. Such property assures the single crystalline nature of the material. In the other hand, an attempt to get information about the thickness of the sheet, we tried to get larger scale of magnification. Fig.4.3 show the magnification by 120000 times of the crystal. Unfortunately, the photos are not clear and obtaining clear image was not possible. For one of the nanosheets we succeed in measuring its thickness. The one-layer thickness is ~ 58 nm. This result indicate that the $Tl_2InGaSe_4$ single crystals are composed of stacked nanosheets that could be easily cleaved. Such property makes the crystal promising for applications in nano-applications.

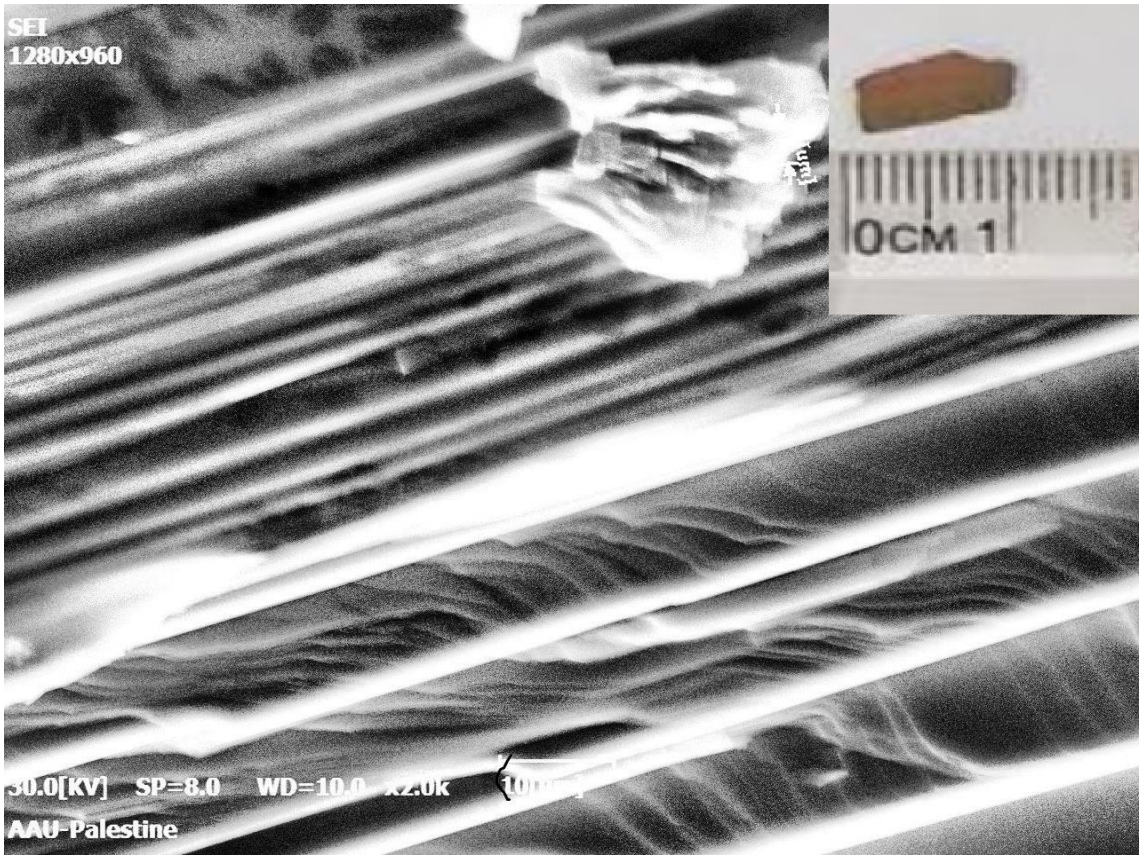

Fig 4.1: Cross-sectional view of the $Tl_2InGaSe_4$ single crystals being recorded by scanning electron microscope with magnification of 2000 times.

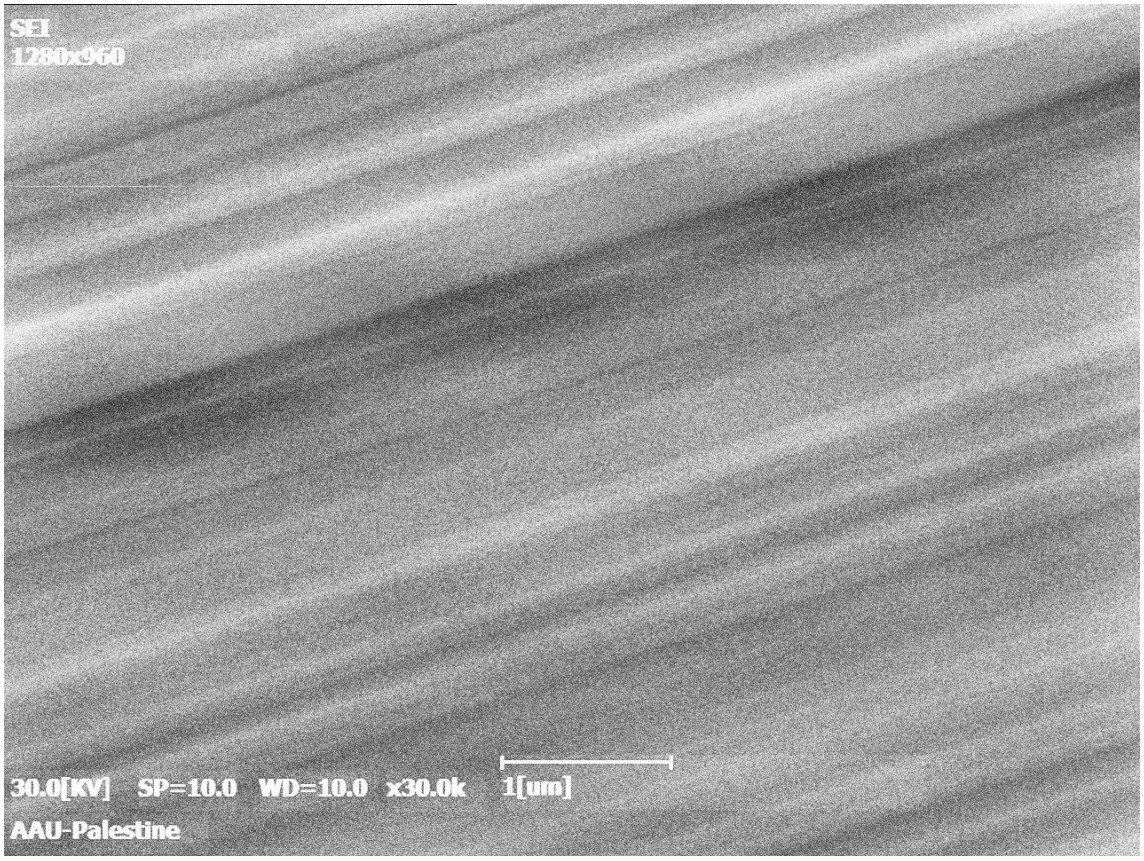

Fig 4.2: Cross-sectional view of the $Tl_2InGaSe_4$ single crystals being recorded by scanning electron microscope with magnification of 10000 times.

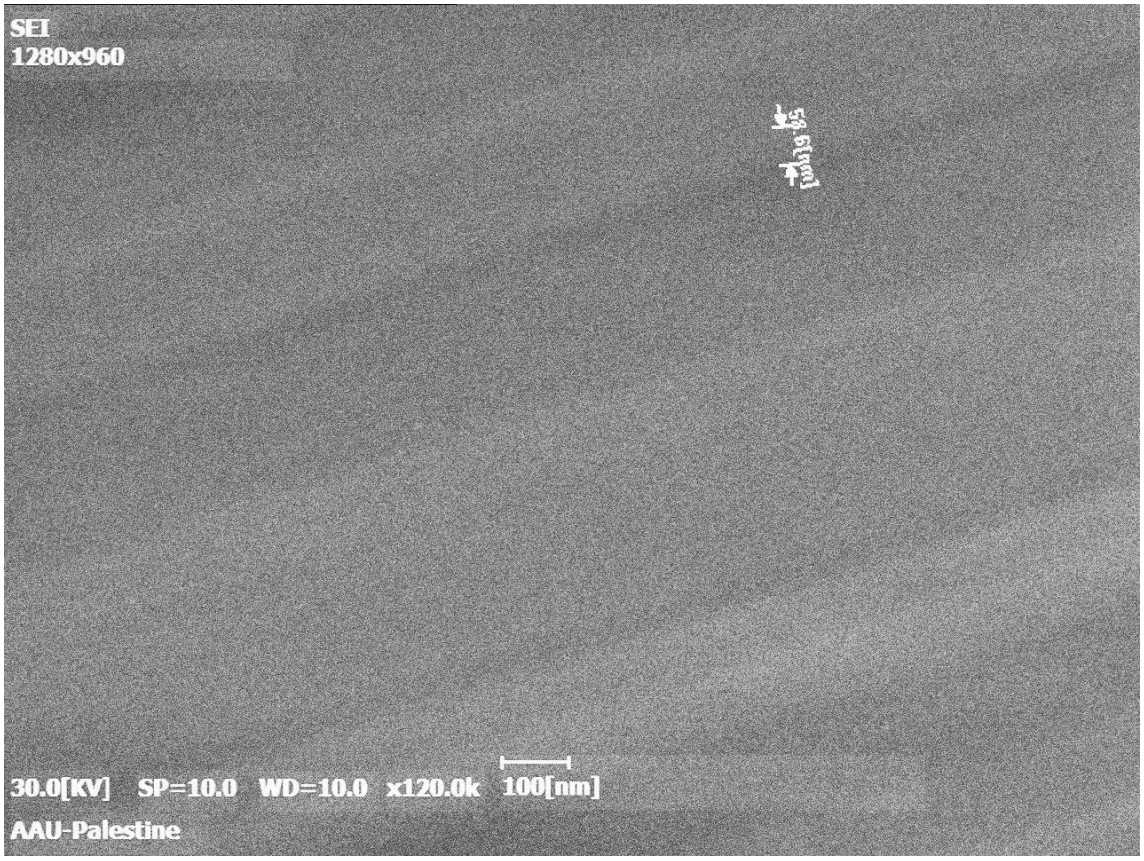

Fig 4.3: Cross-sectional view of the $Tl_2InGaSe_4$ single crystals being recorded by scanning electron microscope with magnification of 120000 times.

4.2 Structural Analysis

The X-ray diffraction (XRD) patterns for $Tl_2InGaSe_4$ crystal in 3D are represented in Fig 4.4 (a). And, in 2D it is represented in Fig.4.4 (b). The XRD patterns are recorded in the temperature range of (298-473K). To investigate the structural type, Treor 92 software package was used. Among the possible solutions, the most appropriate one was related to the monoclinic structure. The lattice parameters of the monoclinic and tetragonal unit cell are found to be a=7.7244, b=6.4945, c=9.2205A^o, β=95.03^o and a = 7.6568, c = 24.060 Å, respectively.

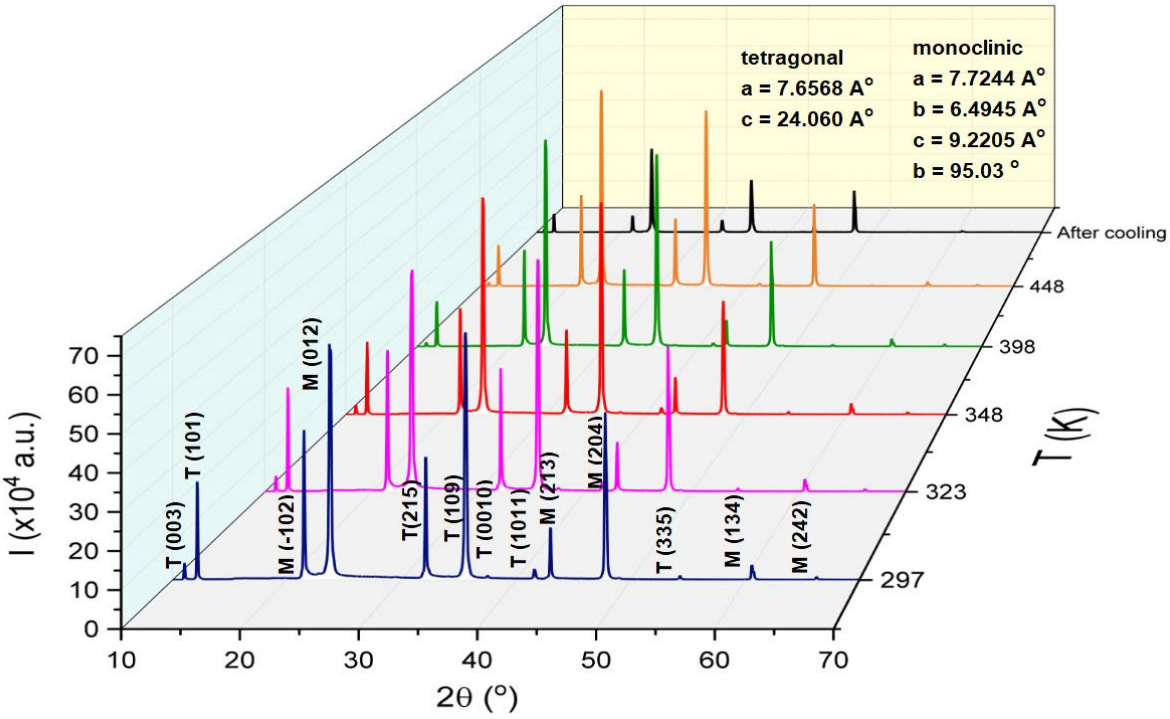

Fig.4.4 (a): The X-ray diffraction patterns for $Tl_2InGaSe_4$ crystal in 3D.

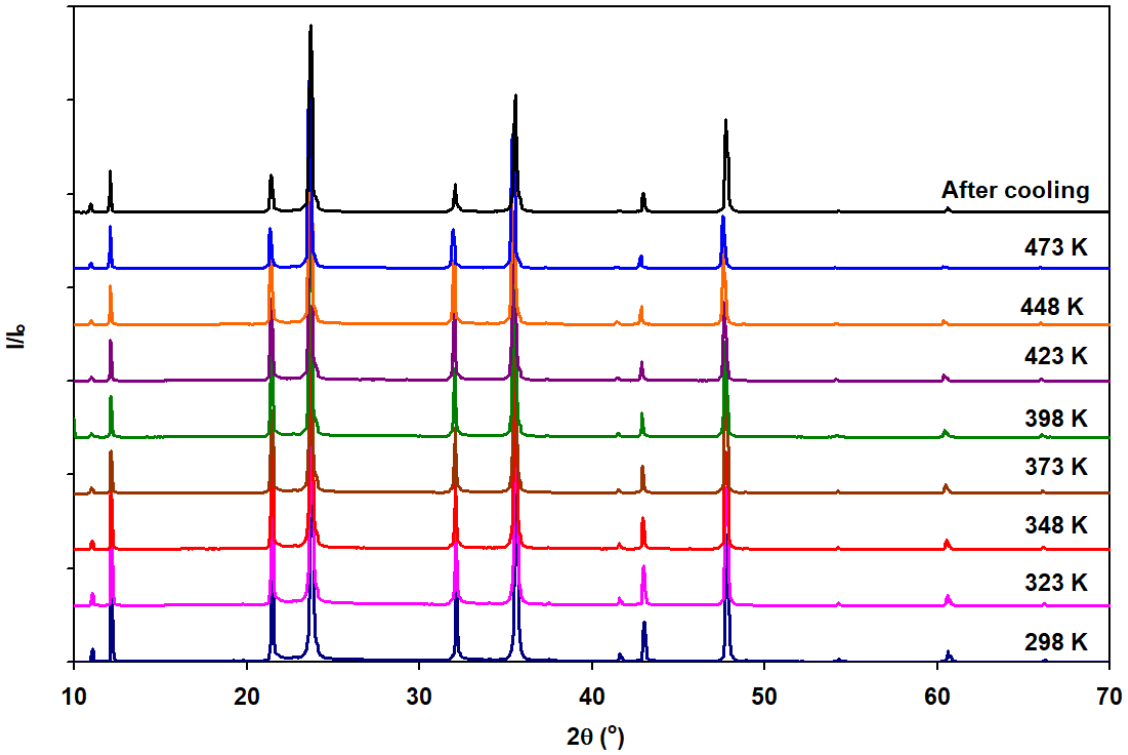

Fig.4.4 (b): The X-ray diffraction patterns for $Tl_2InGaSe_4$ crystal in 2D.

One interesting feature of the peak located at 23.8 ^{o} is the splitting of the peak into two peaks before heating and during heating up to 348K as shown in Fig.4.5 (a). When the temperature value 348K is reached, the two peaks combine and intensive peak is observed. The intensity of this peak increases with increasing temperature. On the other hand, the second peak which was observed at 35.7^{o} (fig.4.5. (b) exhibit an increase in the intensity value with increasing temperature. As demonstrated in Fig.4.6, both peaks exhibit lower intensity values after cooling the samples. In addition, Fig.4.5 compares the XRD patterns of the samples before heating and after cooling, which indicates the disappearance of the peaks which are locked at A, B, C and D marked diffraction angle. In addition, the peak centered at 23.8^{o} become more intensities and of single pattern rather than splitted. This behaviour indicates an improved crystallinity as a result of heating process.

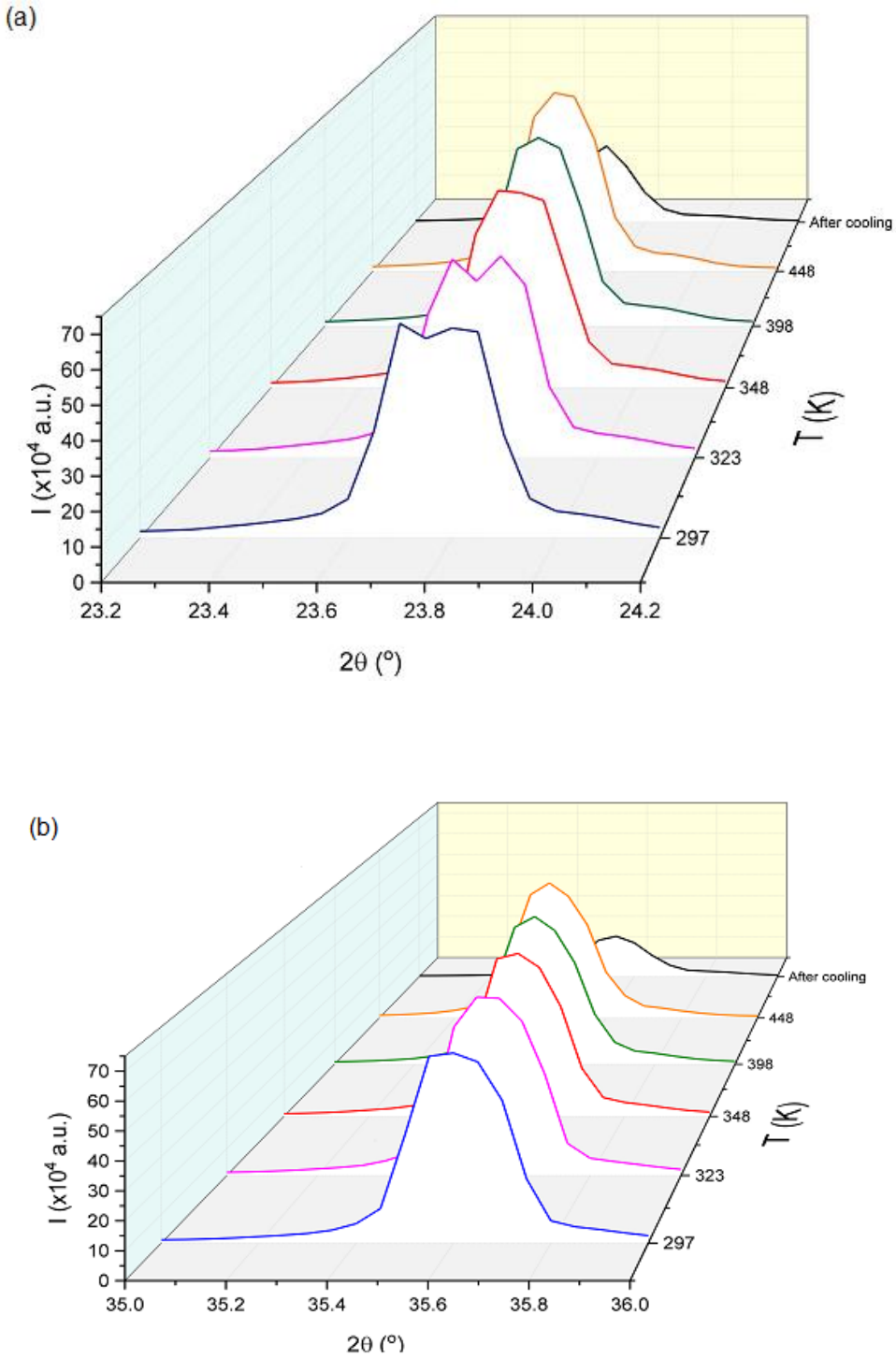

Fig.4.5: The X-ray diffraction patterns for (a) the first maximum peak and (b) the second maximum peak.

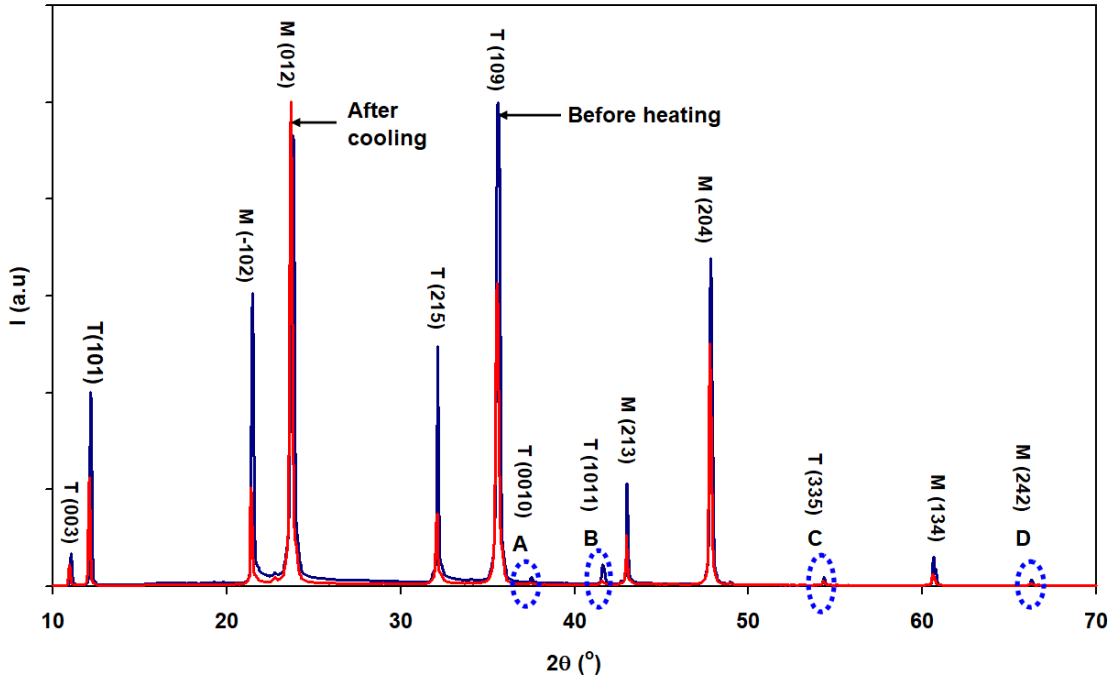

Fig. 4.6: The X-ray diffraction pattern with before heating and after cooling.

The splitting of the peak centered at 23.8° is usually assigned to the presence of more than one phase in the crystal structure.

$Tl_2InGaSe_4$ crystal is composed of the $TlGaSe_2$ and $TlInSe_2$. $TlGaSe_2$ have two layers that are rotated from each other by 90°, $TlGaSe_2$ unit cell structure is monoclinic with parameters of a=7.772, b=10.771 and c=15.636 Å, β=100.06°. As demonstrated in Fig 4.7 (a) by Kashida et al [28], the triangles represent $GaSe_4$ tetrahedral. This tetrahedral is connected to form long Ga_4Se_{10} tetrahedral structure. In Fig 4.7 (b) [29], N.M.Gasanly mentioned that the $Tl_2InGaSe_4$ consists of monoclinic $TlGaSe_2$ and tetragonal $TlInSe_2$. They have chain structures, in which intralayer bonding forms between Tl and Se atoms while interlayer bonding forms between Ga and Se atoms. The basic structural units of a layer $TlGaSe_2$ and $TlInSe_2$ are the $GaSe_4$, and $InSe_2$ polyhedrons respectively. Four elementary $GaSe_4$ tetrahedral linked together by bridging Se atoms for the combination of the fundamental structural unit [29].

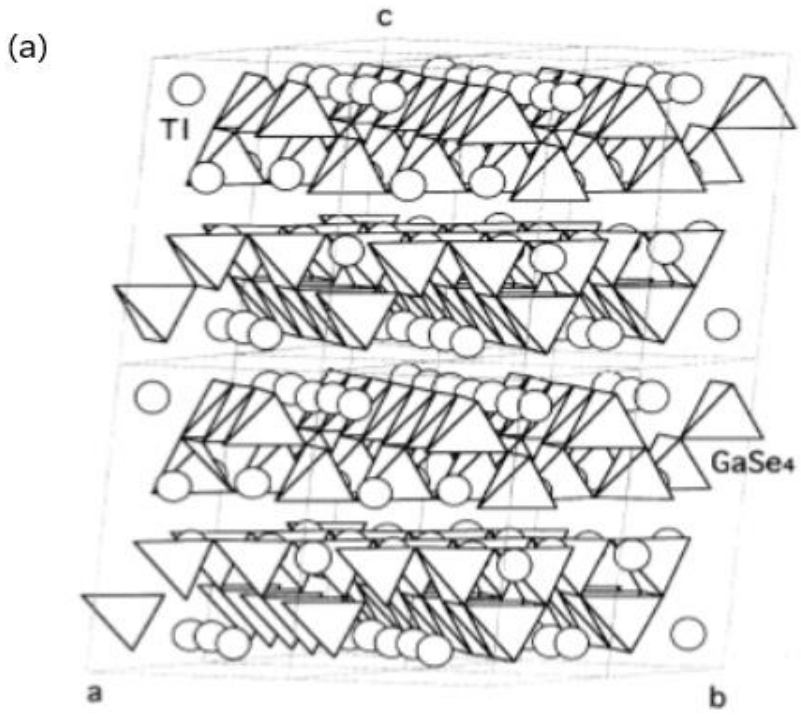

Fig.4.7 (a): As reported by Kashida et al crystal structure of $Tl_2InGaSe_4$[27].

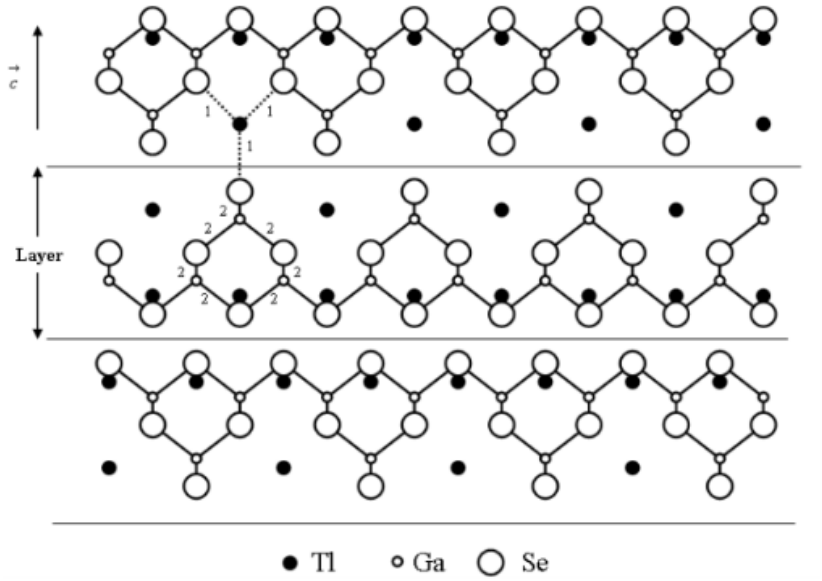

Fig.4.7 (b): As reported by N.M.Gasanly projection of the structure in the$TlGaSe_2$ crystal. the number (1) represents the interlayer bonding between Tl and Se atoms, the number (2) illustrates the intralayer bonding between Ga and Se atoms [29].

On the other hand, $TlInSe_2$ family relates to the TlSe-type structure [30], the coordination number of the monovalent thallium cation is 8 in $TlInSe_2$ as illustrate in Fig 4.8 (a). Ga is contained tetrahedral coordination and dominant covalent bonding.

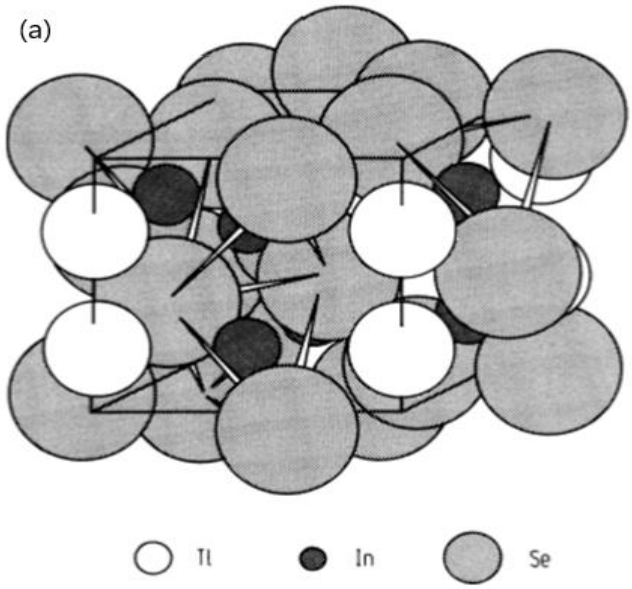

Fig.4.8 (a): The $TlInSe_2$ crystal structure as reported by O.Madelung [30].

D.G.Kilday [31] reported that the $TlInSe_2$ crystal planes are oriented in the [001] direction. $Tl^{+1}(In^{+3}Se_2^{-2})$ is another formula for $TlInSe_2$ compound, which emphasizes that $TlInSe_2$ crystal structure is formed from the chains of trivalent covalently bounded to Se [24]. Fig 4.8 (b) [31] illustrates the crystal structure of the tetragonal $TlInSe_2$ in [001] direction. The square which is at the lower right of the figure represents the projection of the unit cell. The structure of $TlInSe_2$ is composed from a binary compound of TlSe. In this compound Indium atoms are substitutes half of the Thallium atoms.

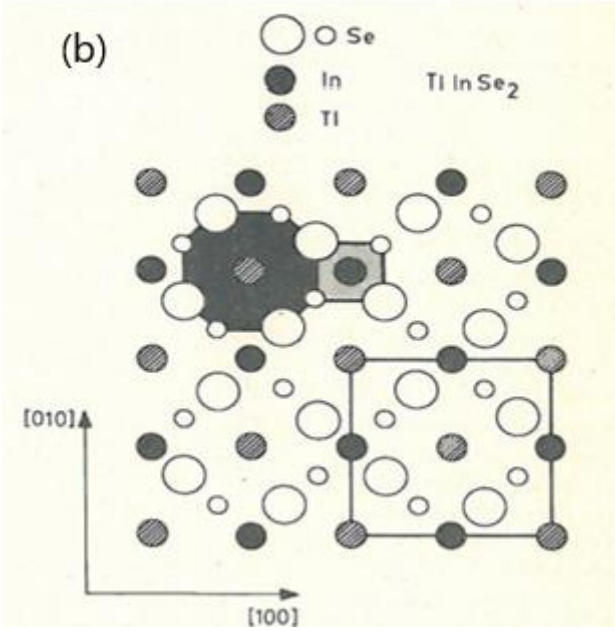

Fig.4.8 (b): The crystal structure of $TlInSe_2$ as reported by D.G.Kilday [31].

With the help of crystal maker soft package, $TlGaSe_2$ and $TlInSe_2$ are designed and shown in Fig 4.9 (a) and (b). The figure shows sites of Tl, Ga and Se atoms in $TlGaSe_2$ crystal structure, also Tl, In and Se atoms in $TlInSe_2$ crystal structure before combination to form $Tl_2GaInSe_4$ crystal structures. The blue color cube in the Fig 4.9 (a) illustrates the monoclinic unit cell for $TlGaSe_2$ and the red color shape represents the clearest plane in this structure. Likewise, Fig. 4.9 (b) explains the unit cell for the tetragonal $TlInSe_2$. The red color hexagonal shaped is the best plane that can be observed clearly more than other planes in that unit cell.

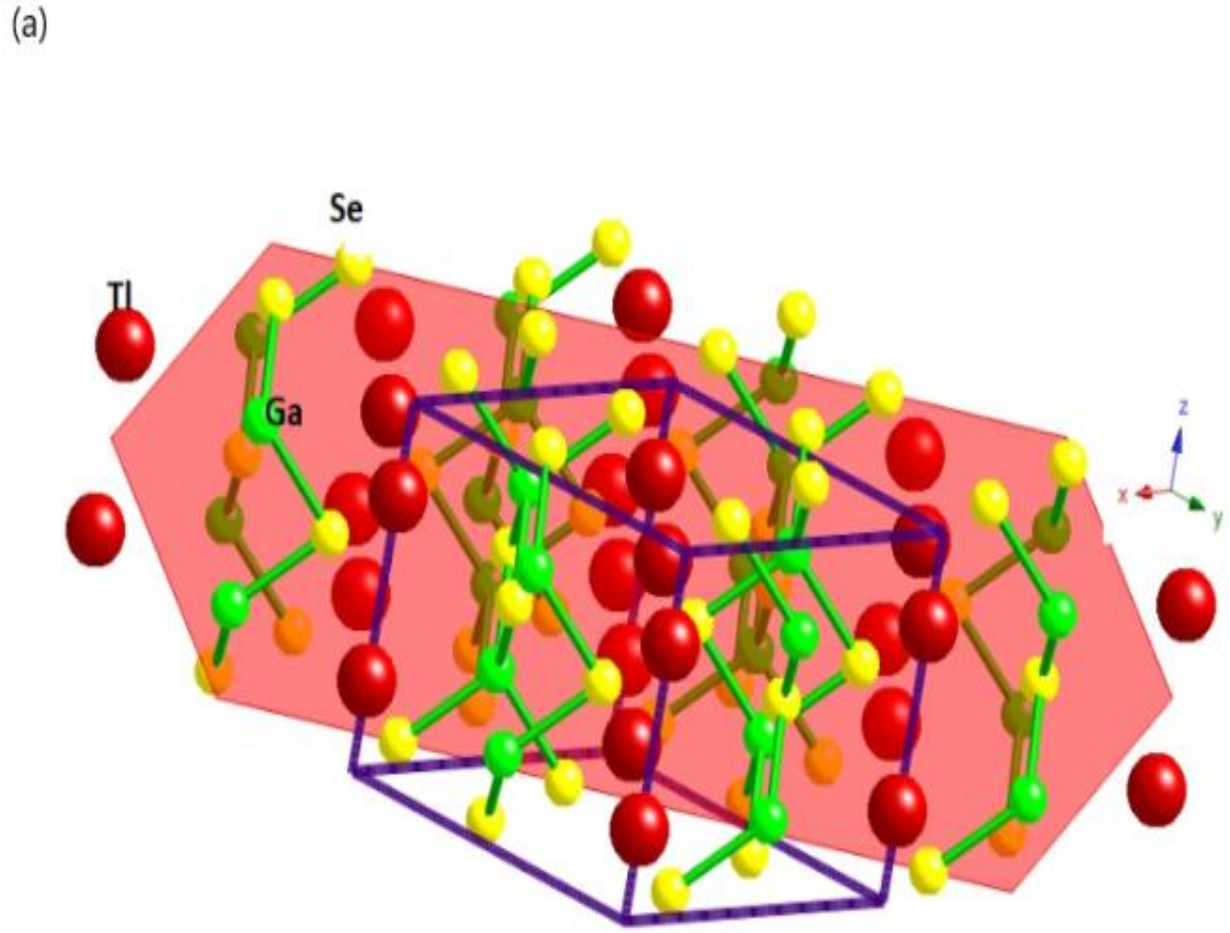

Fig.4.9 (a): Crystal structure for monoclinic $TlGaSe_2$.

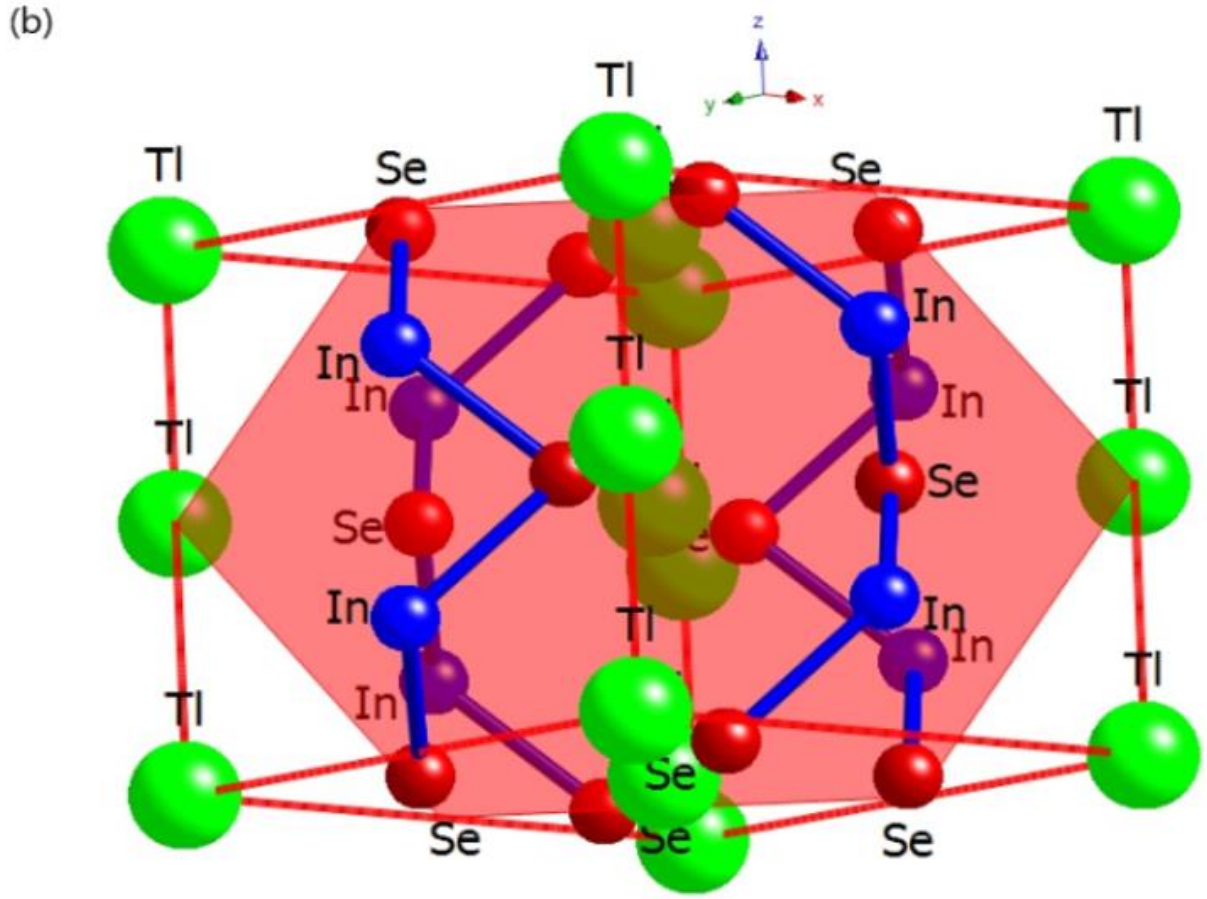

Fig.4.9 (b): The unit cell for the tetragonal $TlInSe_2$.

As shows in Fig. 4.6 (a), at 297, 323 and 348 K, our crystal under study exhibit phase transition from tetragonal to monoclinic due to the preferred atomic plane rotation in the $Tl_2InGaSe_4$ crystals. The plane rotation is assigned to the bonding mechanism and vacancy filling.

Table 1: The bonds in $Tl_2InGaSe_4$ and their length.

Bond	Length (Å)	Ref.
Tl-Tl	2.95	[32]
Tl-In	3.47	[33]
Tl-Se	3.45	[34]
In-Se	2.75	[35]
Tl-Ga	2.50	[36]
Ga-Ga	2.34	[37]
Se-Se	3.51	[38]
Ga-Se	2.39	[34]

As shown in Table 1, the bond length of Tl-Ga is shorter than that of Tl-In. The shorter bond makes the bonding of Tl-Ga preferable over Tl-In. As a result, the monoclinic structural (Tl-Ga) become more dominant over the structure of (Tl-In) which is tetragonal. In addition, as the ionic radius of Ga (187 pm) is less than ionic radius of indium (220 pm), the substitutions of Ga atoms in vacant sites of Indium make the $TlGaSe_2$ monoclinic structural type more dominate over that of $TlInSe_2$ tetragonal under these conditions, $Tl_2InGaSe_4$ would prefer to exhibit the structure of $TlGaSe_2$ rather than that of $TlInSe_2$.

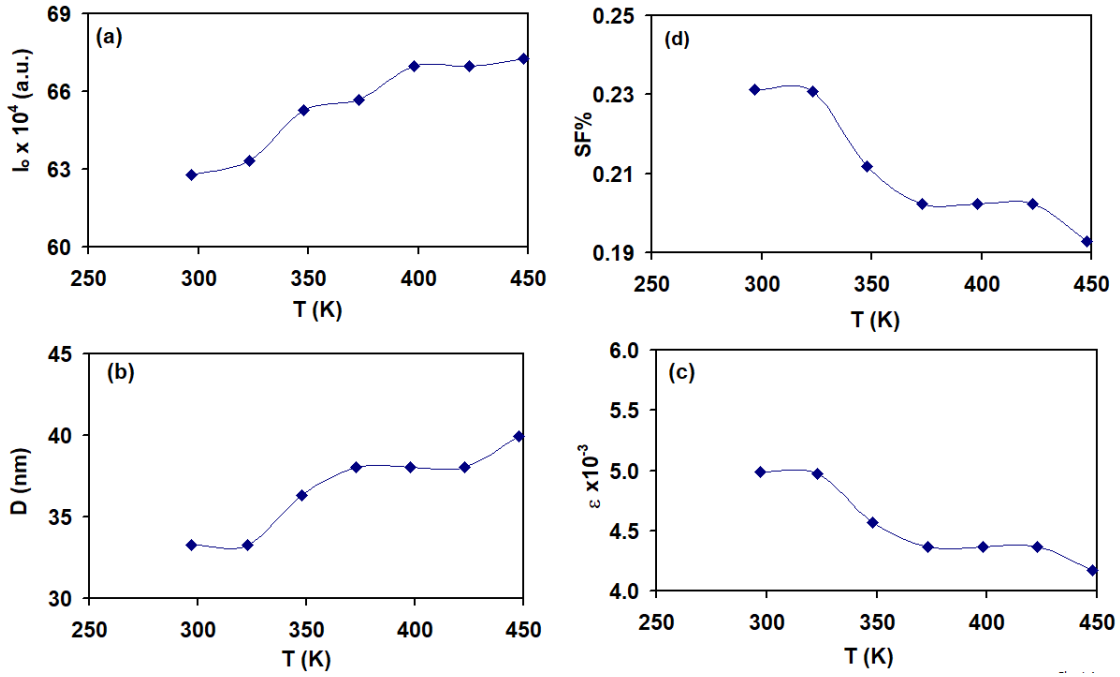

Fig. 4.10: The temperature dependent (a) intensity, (b) crystallite size(D), (c) strain (ε)and (d) stacking faults (SF) for the $Tl_2GaInSe_4$ crystal.

Fig 4.10 (a) - (d) represents the (a) intensity, (b) crystallite size(D), (c) strain (ε) and (d) stacking faults (SF) variations with temperature for the maximum peak.

The D, ε and SF are calculated from the broadening width (β), for the most intensive peak, through the eq. (2.14), eq.(2.15) and eq.(2.16).

Fig.4.10 (a) shows the enhancement of the main peak intensity upon heating. Particularly, the intensity increased from $62x10^4$ at 297 K to $67x10^4$ at 450 K. It indicates well oriented planes. In addition, the crystallite size which is shown in Fig.4.10 (b) follow the same trend of variation. The crystallite size increased from 33 to 40 nm. In Fig.4.10 (c) and (d), the strain and the stacking faults are decreased, respectively. The decrease in the number of wrongly located atoms presented by stacking faults accepts both of the preferred bonding and ionic substitution mechanisms as a reason for the structural transformations [39].

4.3 Optical Analysis

The spectral data of transmittance (T) for the $Tl_2InGaSe_4$ crystals in the incident wavelength (λ) range of 300-1100 nm is shown in Fig. 4.11. The figure shows, the transmittance values, which highly sensitive to the varying temperature. Particularly, increasing the temperature lead to in the decreases the transmittance. The decrease in the transmissivity is accompanied with shift in the high transmittance edge. On the other hand, the absorption coefficient (α) which is calculated from the measured transmittance through the relation $\alpha = \ln\left(\frac{1}{T}\right)$, exhibit an opposite behavior. Namely, the absorption coefficient values increase with increasing photon energy and temperature.

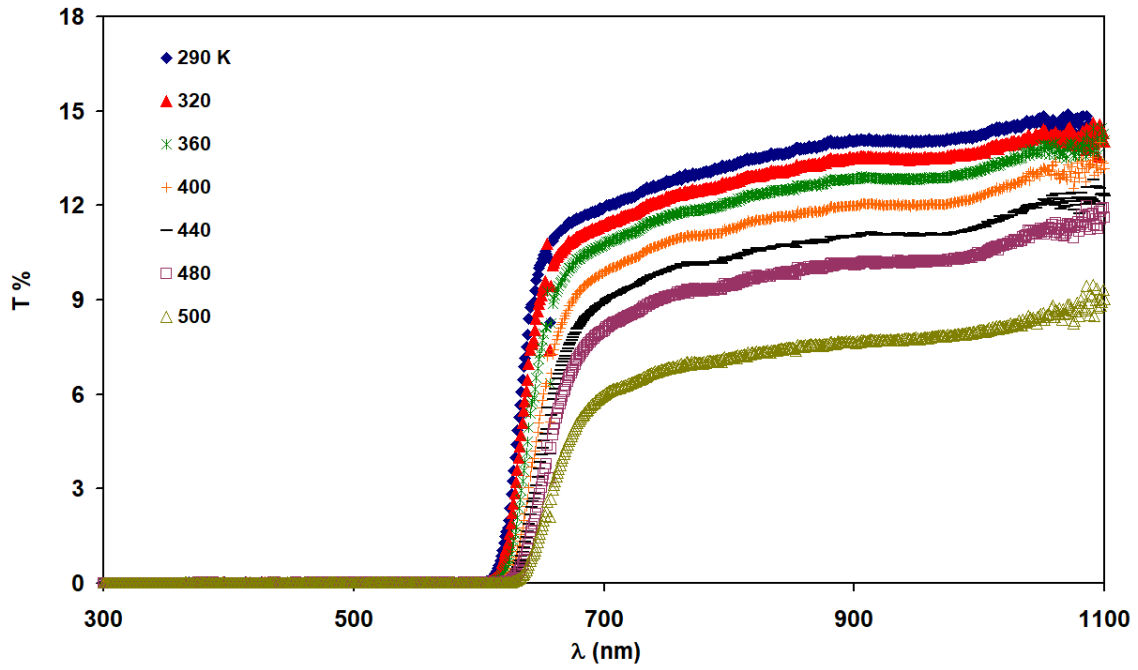

Fig. 4.11: The transmittance with wavelength.

The temperature dependence of the absorption coefficient for $Tl_2InGaSe_4$ single crystal is illustrated in Figure 4.12. It is observed that the absorption coefficient of $Tl_2InGaSe_4$ also shifts toward lower energy values as the temperature is increased. The significance of the absorption coefficient (α) is to get usability information about the energy band.

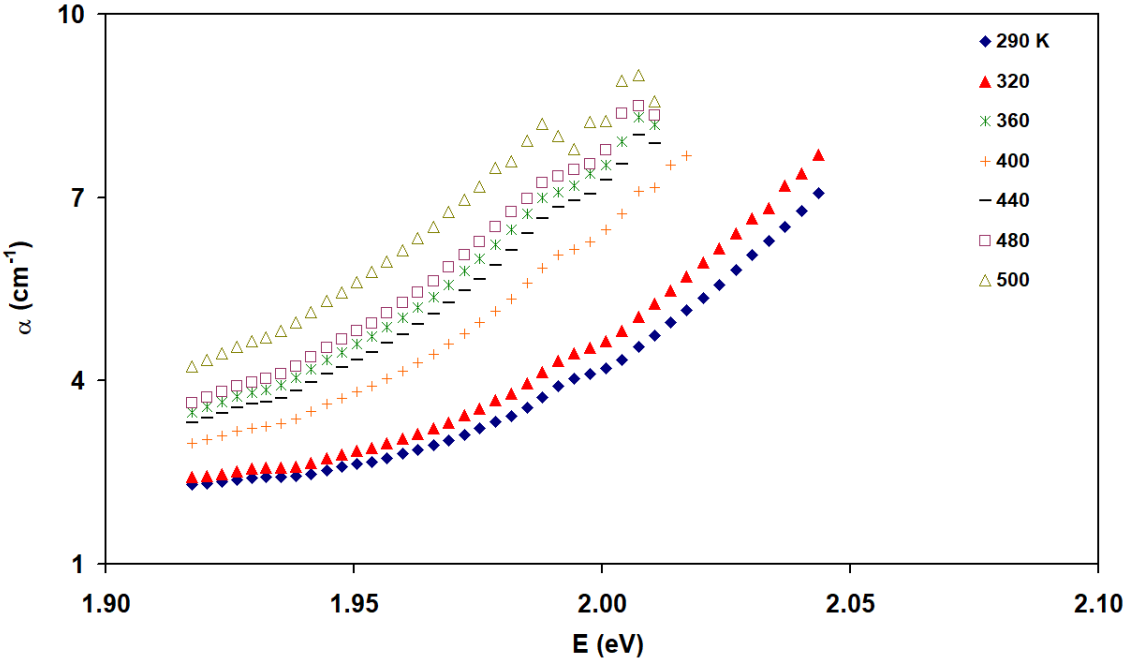

Figure 4.12: Temperature dependence of the absorption coefficient for Tl_2InGaS_4 crystal.

From the data which are shown in Fig. 4.12 we have obtained values of the direct and indirect allowed transition energy band gap (E_g) through Tauc's equation. Particularly, applying Tauc's equation $(h\nu)^p$ = (E-E_g) to plot $(\alpha E)^p$ –E, where p characterizes the optical absorption process. Theoretically, direct allowed electronic transitions equal 2 as in Fig 4.14 and Fig.4.15 for indirect allowed electronic transitions as shown in Fig 4.15 (b) where p = 1/2. There's possible to explore the temperature effects on the energy band gap.

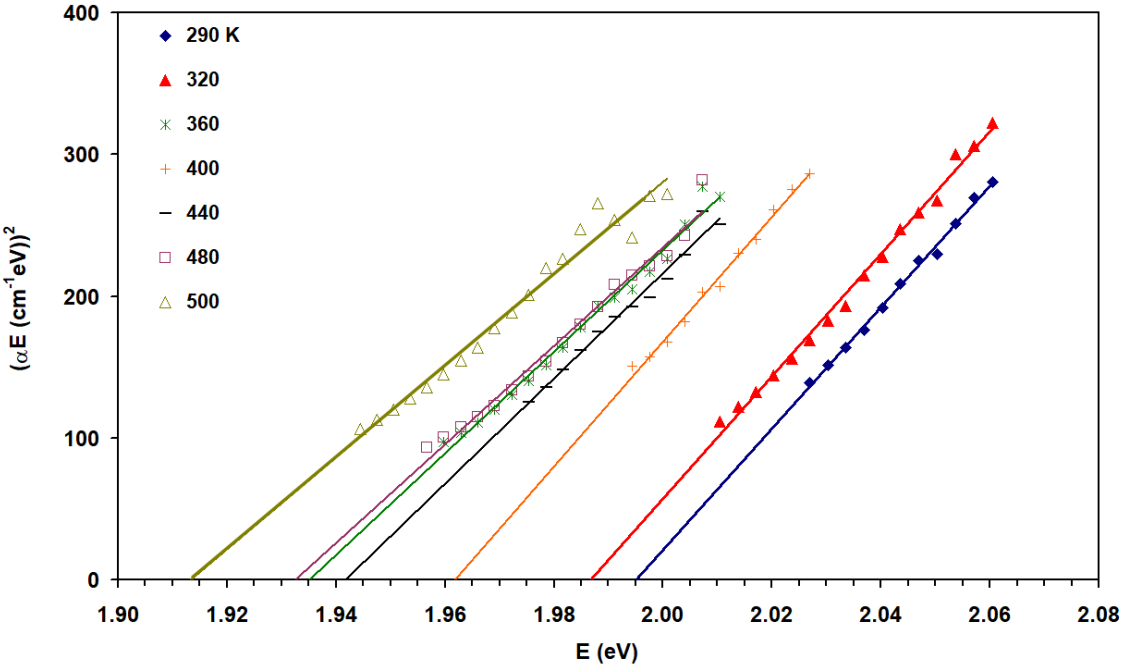

Figure 4.13: The $(\alpha E)^2$–E plots at selected temperatures.

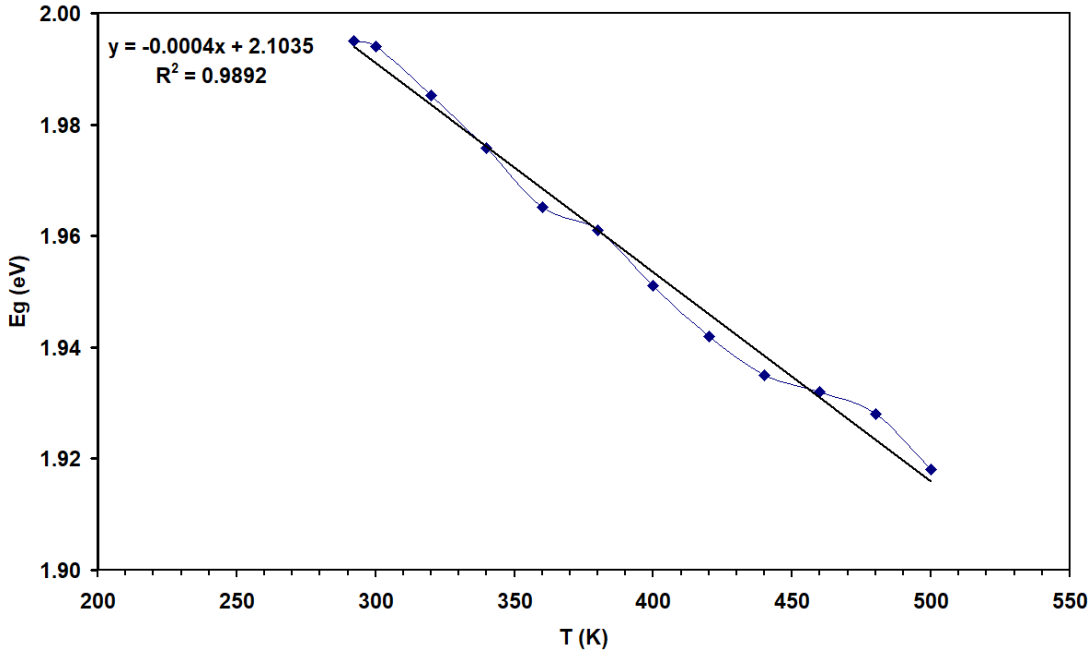

Figure 4.14: The direct energy band gap as a function of temperature. The solid line represents the fit using Tauc's equation.

As illustrated in Fig. 4.14, when the temperature increased the value of direct a In other word, it decreases from 1.99 to 1.91 eV as temperature increases from 292 to 500 K.

The temperature dependence of the energy band gap can be represented by the relation (4.1) [40]:

$$Eg\ (T)\ =\ E_g\ (0) + \gamma T^2/(T + \beta) \qquad (4.1)$$

In this equation, E_g (0) is the absolute zero value of the band gap, $\gamma\ =\ dE_g/dT$ is the rate of change of the band gap with temperature and β is Debye temperature, which approximately equals 65 K for $Tl_2InGaSe_4$ crystals.

The fit of equation (4.1) which is shown by solid line in Fig. 4.13 reveal the equation parameters as E_g (0) = 2.1eV and $\gamma\ =\ -9.5\ \times\ 10^{-4} eV\ K^{-1}$.

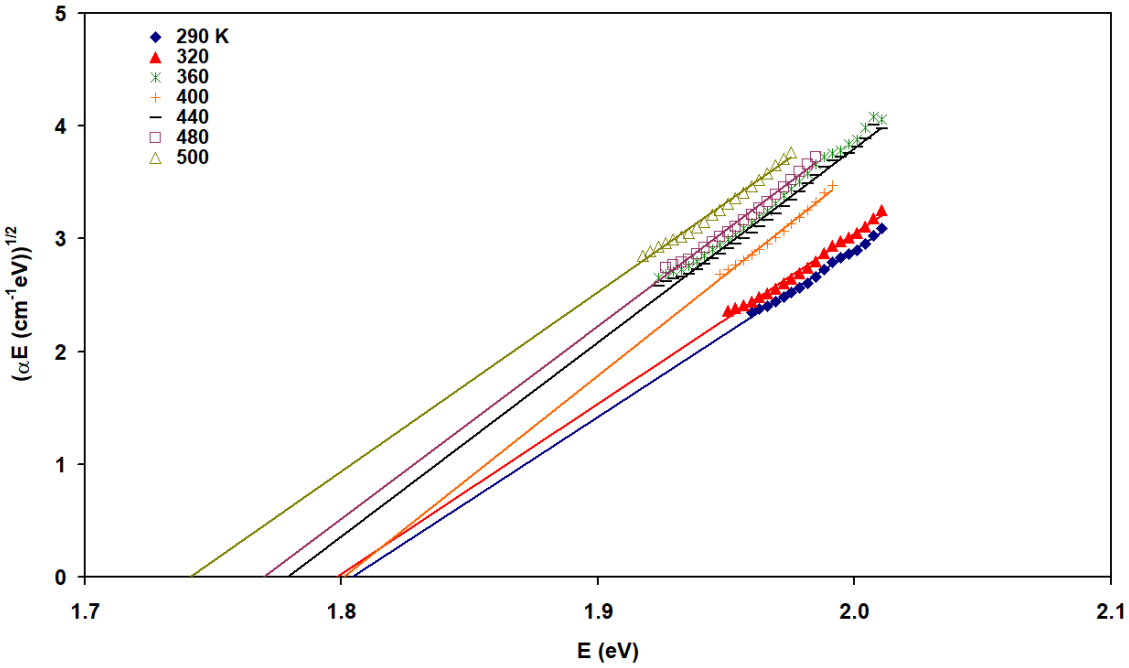

Figure 4.15: The $(\alpha E)^{1/2}$–E plots at selected temperatures.

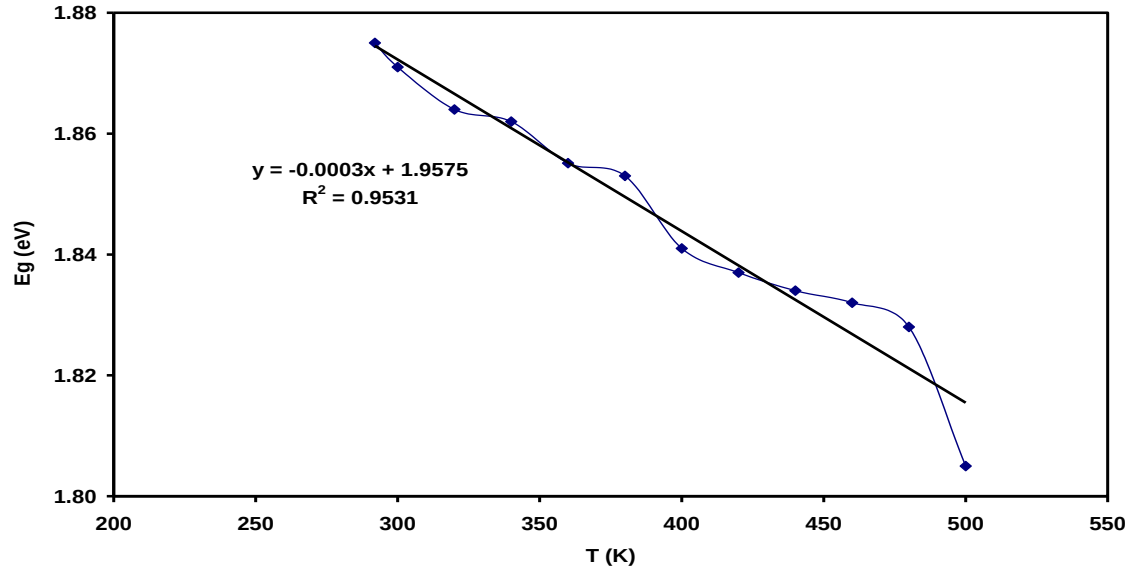

Figure 4.16: The indirect energy band gap as a function of temperature. The solid line represents the fit using Tauc's equation.

Figure 4.16 illustrates the behavior of the indirect energy band gap Vs temperature in which we obtained the values of the indirect and direct gap from the E-axis crossings in

the linear region of the α-E variation. The figure displays the value of E_{gi} which decreases with increasing temperature. Namely, it shifts from 1.875 to 1.805 eV as temperature increases from 292 to 500 K. The fitting of equation 4.2 for indirect gap – temperature variation reveals the same E_g (0) and β values.

The changes in the energy band gap value with temperature is assigned to the changes in crystallite size, lattice constant and stacking fault with temperature. The rising in the temperature which causes the decreasing in the energy band gap value is assigned to extension of the crystallite size which relates to compressing strain and less stacking faults [41,42]. In addition, a relaxation of the residual stress as a result of decrease in the lattice constant with temperature rising. Interstitial atoms and vacancies cause stresses; at the normal sites of the lattice [43,44]. The interstitial atoms are eliminated leading to the enlargement of lattice parameters and hence causing compressive stress [40].

4.4 Current- Voltage Characteristics

The current (I)-voltage (V) characteristics is a main tool to investigate the performance of devices and is a method used to measure the barrier heights of a metal-semiconductor contacts [45,46]. The barrier heights are illustrative values for metal-semiconductor contacts made by precipitation of high-purity metals in a good vacuum system onto chemically cleaned semiconductor surfaces [17,47].

For $Tl_2InGaSe_4$ crystal Ag and C metal-semiconductor point contacts are used to construct schottky diodes. The I-V data for Ag/ $Tl_2InGaSe_4$/C is recorded in the dark and under various light intensities using a tungsten lamp. Fig. 4.17 illustrates the current-voltage characteristics for Ag/ $Tl_2InGaSe_4$/C device. As it is observed from the figure, the current values under forward biasing conditions are higher than those in the reverse biasing. Theoretically, it is difficult to decide whether the device under investigation is back to bake Schottky or Schottky type [48,49], due to the lack information about the electron affinities of $Tl_2InGaSe_4$.

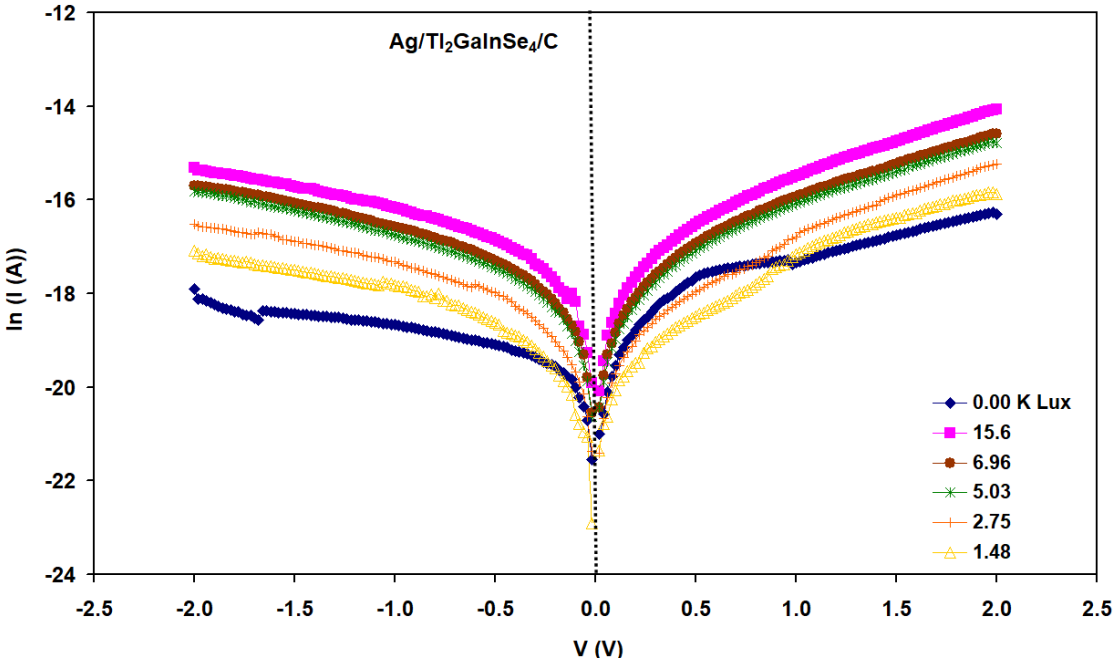

Fig.4.17: The current-voltage characteristics for the Ag/ $Tl_2InGaSe_4$/C diode.

Because of the rectifying properties of the I-V characteristics, the Schottky-Richardson approach for current conduction was carried out in details. In this approach, the current injection is controlled by the thermionic emission of charge carriers over a barrier height (ϕ_b) [8]. The Richardson-Schottky current is given by the equation [8],

$$I = AA^*T^2 exp\left(\frac{-q\phi_b}{KT}\right)\left(exp\left(\frac{qV}{nKT}\right) - 1\right) \quad (4.2)$$

Where A is the area of diode, $A^* = 120$ m* is Richardson constant, m* = 0.24 m_o is the effective mass for $Tl_2InGaSe_4$ [7], n is the ideality factor. Figure 4.17 (a) and (b) show the current-voltage characteristic under forward and reverse biasing conditions. The relation between ln (I_R) and ln (I_F) with V is approximately, linear. Meaning the validity of eq. (4.2). It is also noticeable from the figure that the forward current values are higher than reverse current in the dark.

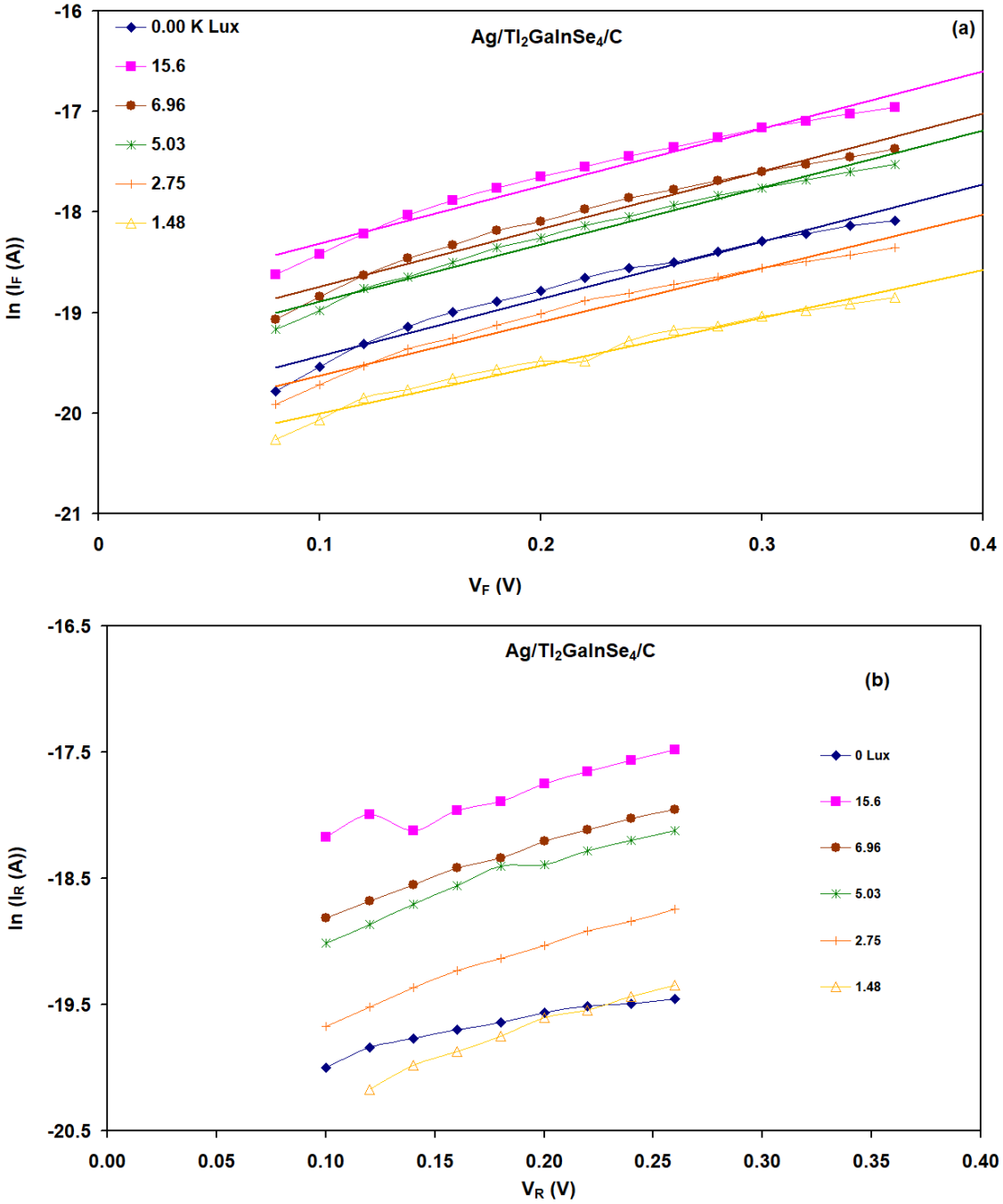

Fig.4.18: The current voltage characteristics for the Ag/ $Tl_2InGaSe_4$ /C diode, (a) under forward and (b) reverse biasing condition.

From the slopes, and the intercepts of the linear plots which are shown in Fig 4.18 (a) and (b) and with the help of equation (4.2), the ideality factor and barrier height were calculated. Executing the exponent of equation (4.2) one may reveal the form.

$$\ln(I) = (\ln(AA^* T^2) - \frac{q\phi_b}{KT} - \frac{qV}{4KT} \quad (4.3)$$

In equation (4.3), the slopes of the ln (I) – (V) variations which are shown in Fig. 4.19 reveal the ideality factors and the intercepts reveal the barrier heights. The calculated ideality factors and barrier heights are shown in Fig. 4.19. As seen from Fig. 4.19 (a), the ideality factor is larger than one and exhibit random behavior in response to light intensity. On the other hand, the barrier height systematically decreases with increasing light intensity. No significant difference between the forward and reverse biased barrier heights can be detected. The deviation of ideality factor from unity may be assigned to many reasons like, surface inhomogeneities, defects, generation-recombination mechanisms and series resistance effect [8].

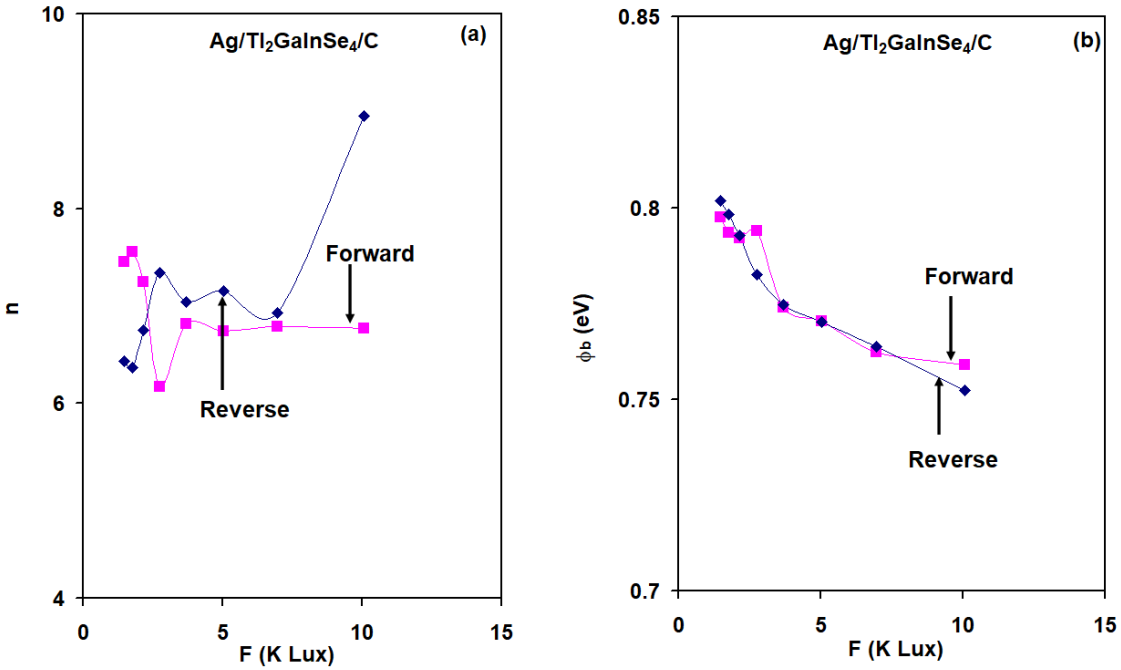

Fig.4.19: (a) The ideality factor and (b) the barrier height – light intensity dependencies for Ag/ $Tl_2InGaSe_4$ /C diode.

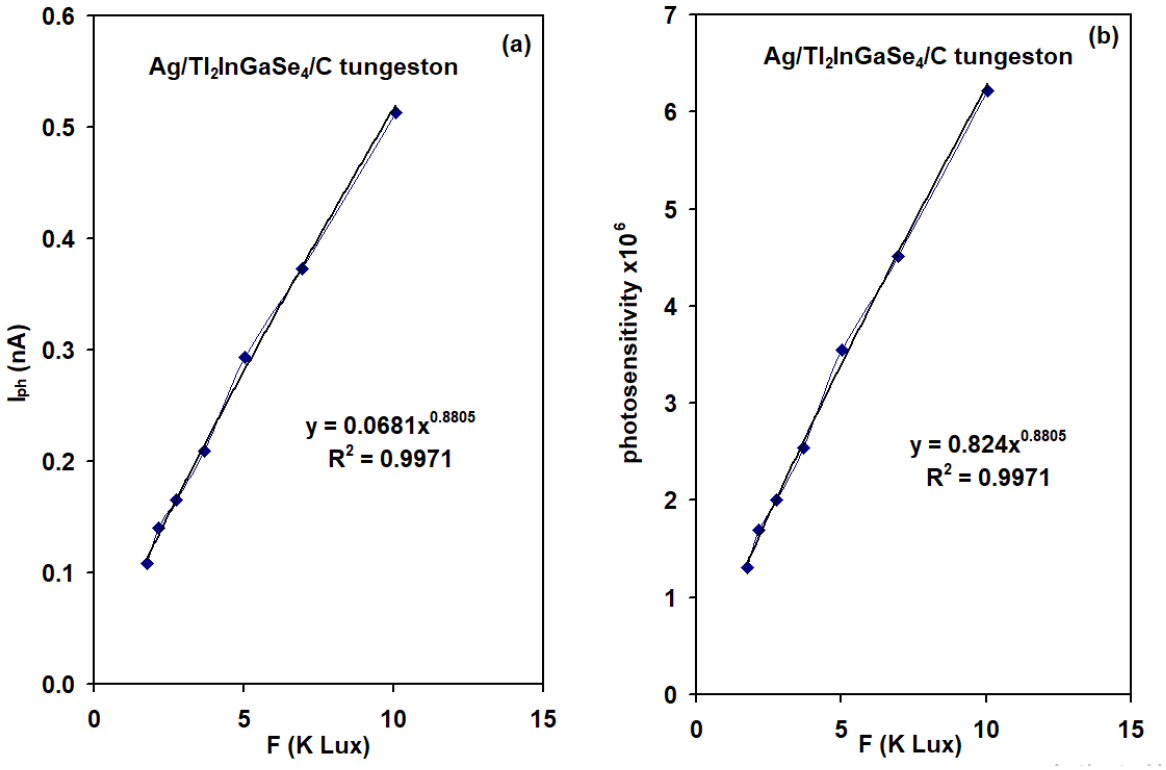

Fig.4.20: The light intensity dependence of the (a) photocurrent and (b) photosensitivity for the $Ag/Tl_2InGaSe_4/C$ devices.

To explore the ability of the $Ag/Tl_2InGaSe_4/C$ crystal, to detect light, the photocurrent ($I_{ph} = I_L - I_d$) is extracted from the difference between the measured light and dark current. The photocurrent as function of light intensity is shown in Fig. 4.20 (a). As seen I_{ph} linearly increases with increasing intensity. It indicates that there is linear recombination process in the bulk of the samples. In addition, the device photosensitivity (S) is calculated from the relation (4.5) [8],

$$S = \frac{I_{ph}}{I_d} \qquad (4.5)$$

and plotted in Fig. 4.20 (b), the photosensitivity increases with increasing intensity. It reaches values of $6.2x10^6$ at 10 K Lux. This remarkable value is important as it indicate applicability of crystals in optoelectronics as photodetector.

4.5 Impedance spectroscopy

The spectral range which is used to measure the impedance of is the $Ag/Tl_2InGaSe_4/C$ 0.01-1.8 GHz. The resulting capacitance (C) spectra are shown in Fig. 4.21. The figure represents the behavior of capacitance, which vary slowly with frequency at 0.868 GHz, then, continuously decreases following fluctuating mode. The reason for the signal fluctuating shape in this figure is believed to the layered nature of the crystal, as was shown in the SEM image Fig.4.1 and 4.2.

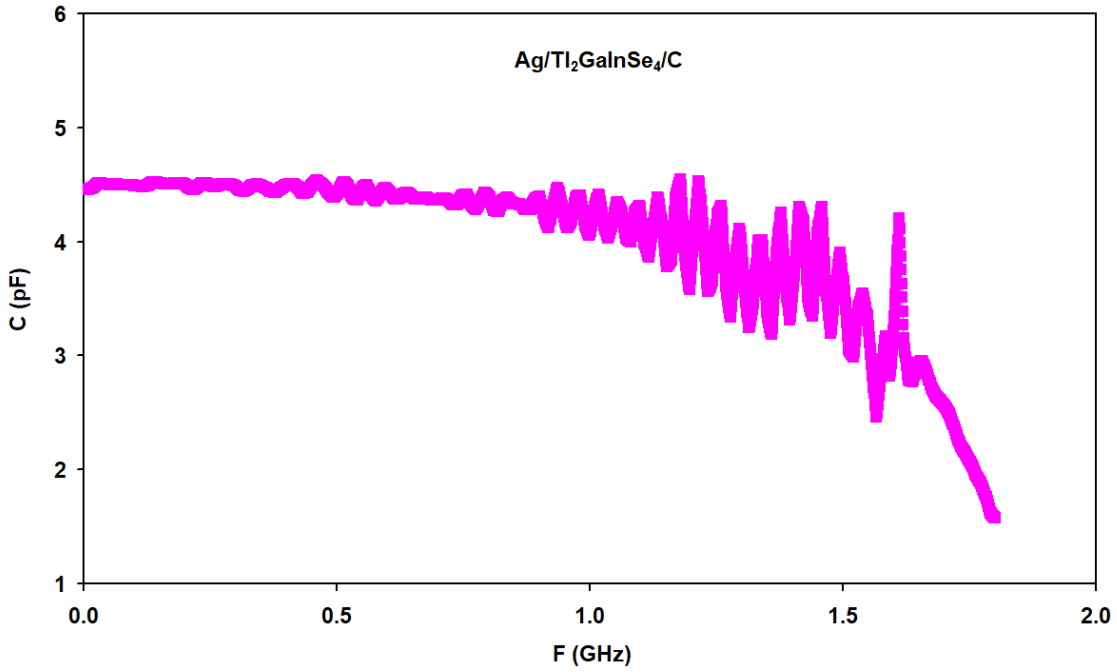

Fig. 4.21: The capacitance spectra for the $Ag/Tl_2InGaSe_4/C$ device.

As seen in Fig. 4.22, which displays the impedance spectra (Z) for the Ag/$Tl_2InGaSe_4$/C device. Z is sharply decreasing from 10^3 to 10^2 Ω. In the range of 0.01-0.5 GHz, the variation decreases slowly until arrived at1.5 GHz exhibiting low values.

The tunability of the capacitance and impedance with single frequency indicates its applicability as variable capacitor suitable for many optoelectronic applications [50,51].

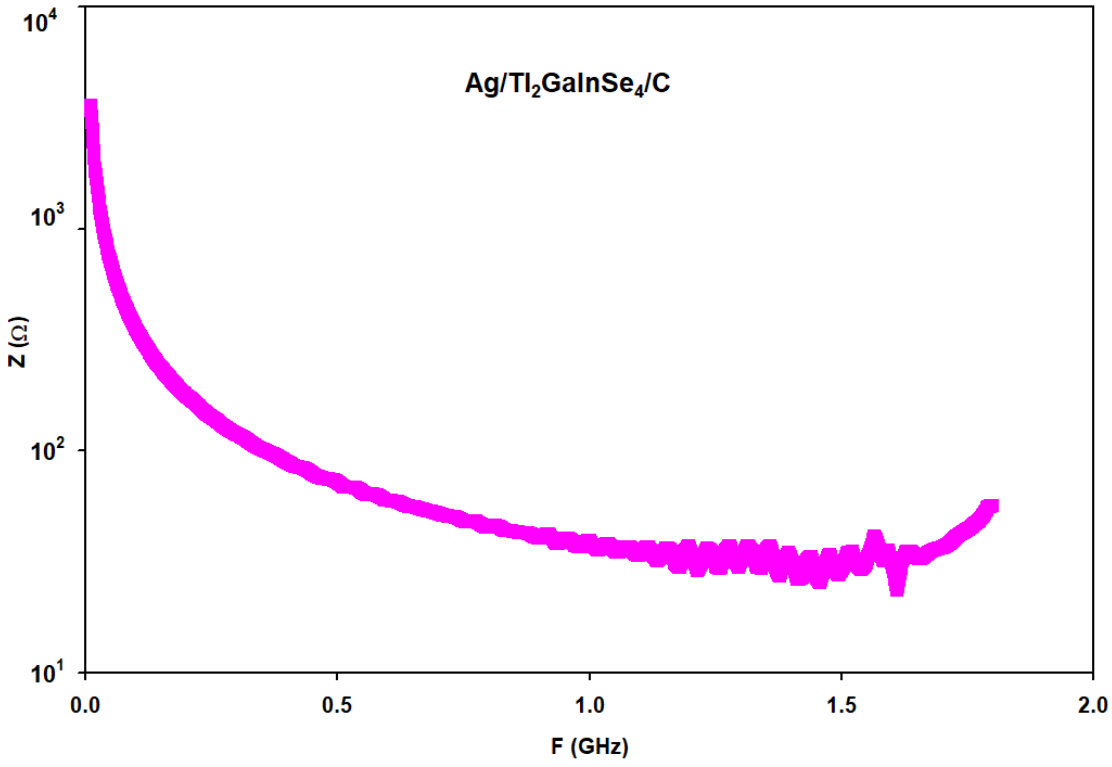

Fig. 4.22: The impedance for the Ag/Tl2InGaSe4/C device.

Chapter Five

Conclusion

In this thesis we targeted explanation of the physical properties of $Tl_2InGaSe_4$ single crystals. The crystal which is prepared by the modified Bridgman technique is composed of 50% $TlInSe_2$ and 50% $TlGaSe_2$. In the SEM analysis technique there very denes layers easily distinguishable from each other. The thickness of layer in nanometer are used for nano-application. The temperature dependent X-ray analysis on the crystals have shown that it exhibits both of monoclinic and tetragonal structures. The heating of the crystals to 473 K and recooling it make the monoclinic phase more dominant over the tetragonal. Optically, the temperature dependent bandgap studies have shown that the energy band gap shrunk a rate of change of $\sim 10^{-4}$ eV/K upon heating. In addition, as practical applications, the crystals are employed to design a schottky barrier device which can be used as a photo sensor. The illumination dependent Current-Voltage studies has shown that the crystals exhibit high photosensitivity up to $\sim 10^6$ under tungsten light illumination. Furthermore, the impedance spectroscopy analysis has shown that the crystals can be used as variable frequency capacitors and could be used as microwave traps.

Reference

[1] Qasrawi, A. F., and N. M. Gasanly. "Space-charge-limited currents and photoconductive properties of Tl2InGaSe4 layered crystals." Philosophical Magazine 88.22 (2008): 2899-2906.

[2] Sardarly, R. M., et al. "Superionic conductivity and switching effect with memory in TlInSe 2 and TlInTe 2 crystals." Semiconductors 45.11 (2011): 1387-1390.

[3] Özgen, Canan. OPTICAL PROPERTIES OF SOME QUATERNARY THALLIUM CHALCOGENIDES. Diss. MIDDLE EAST TECHNICAL UNIVERSITY, 2008.: 3-20.

[4] TlInGaSe Qasrawi, A. F., and N. M. Gasanly. "Space-charge-limited currents and photoconductive properties of Tl2InGaSe4 layered crystals." Philosophical Magazine 88.22 (2008): 2899-2906.

[5] TlGaSe Isaacs, T. J. "Crystal data for thallium gallium diselenide, TlGaSe2." Journal of Applied Crystallography 6.5 (1973): 413-414.

[6] Mahfoud, Hafez, Stefan Wanke, and Christoph Neinhuis. "A Survey of Leaf Epicuticular Waxes and Trichomes in the Genus Aristolochia (Aristolochiaceae) using Scanning Electron Microscopy (SEM).Vol 5" SSRG Int. J. Agriculture & Environ. Sci(2018): 120-131.

[7] Pflugrath, J. W. "The finer things in X-ray diffraction data collection." Acta Crystallographica Section D: Biological Crystallography 55.10 (1999): 1718-1725.

[8] Kumar, Challa SSR, ed. X-ray and Neutron Techniques for Nanomaterials Characterization. Springer Berlin Heidelberg, 2016.

[9] Kacher, Josh, et al. "Bragg's Law diffraction simulations for electron backscatter diffraction analysis." Ultramicroscopy 109.9 (2009): 1148-1156.

[10] Taleb,M.F. and A.F.Qasrawi, “engineering the optical and electrical conduction parameters of ZnSe this film via YAu alloy nanosandwiching”, Arab American University – palestine (2018) 12-13.

[11] Holzwarth, Uwe, and Neil Gibson. "The Scherrer equation versus the'Debye-Scherrer equation'." Nature nanotechnology 6.9 (2011): 534.

[12] Tumuluri, Anil, K. Lakshun Naidu, and KC James Raju. "Band gap determination using Tauc’s plot for LiNbO3 thin films." Int. J. Chem. Tech. Res 6.6 (2014): 3353-3356.

[13] Pankove, Jacques I. Optical processes in semiconductors. Courier Corporation, 2012.

[14] Hamada, Madoka. "Wavelength tunable semiconductor laser light source." U.S. Patent No. 5,970,076. 19 Oct. 1999.

[15] Bakshi, AV Bakshi UA. Electrical circuit analysis. Technical Publications, 2008.

[16]Atangana, Abdon, and Juan Jose Nieto. "Numerical solution for the model of RLC circuit via the fractional derivative without singular kernel." Advances in Mechanical Engineering 7.10 (2015): 1687814015613758.

[17] Sze, Simon M., and Kwok K. Ng. Physics of semiconductor devices. John wiley & sons, 2006.’’

[18] Lakshminarayanaiah, N. "Transport Processes in Membranes: A." Subcellular Biochemistry 6 (2012): 401.

[19] The schottky diode Cheung, S. K., and N. W. Cheung. "Extraction of Schottky diode parameters from forward current-voltage characteristics." Applied Physics Letters 49.2 (1986): 85-87.

[20] Padovani, F. A., and R. Stratton. "Field and thermionic-field emission in Schottky barriers." Solid-State Electronics 9.7 (1966): 695-707.

[21] Nather, R. Edward, and David S. Evans. "Photoelectric measurement of lunar occultations. I. The process." The Astronomical Journal 75 (1970): 575-582.

[22] Schöll, Eckehard. Nonequilibrium phase transitions in semiconductors: self-organization induced by generation and recombination processes. Vol. 35. Springer Science & Business Media, 2012.

[23] Wu, Feng, et al. "AsP/InSe Van der Waals Tunneling Heterojunctions with Ultrahigh Reverse Rectification Ratio and High Photosensitivity." Advanced Functional Materials 29.12 (2019): 1900314.

[24] Qasrawi, A. F., Areen AM Atatreh, and N. M. Gasanly. "Characterization of TlInS1. 8Se0. 2 as advanced functional crystals." Materials Science in Semiconductor Processing 87 (2018): 174-180

[25] Malykhin, Sergei, et al. "Formation of GeV, SiV, and NV Color Centers in Single Crystal Diamond Needles Grown by Chemical Vapor Deposition." physica status solidi (b) (2019): 1800721.

[26] Benck, Jesse D., et al. "Apparatus for operando x-ray diffraction of fuel electrodes in high temperature solid oxide electrochemical cells." Review of Scientific Instruments 90.2 (2019): 023910.

[27] Meuret, S., et al. "Complementary cathodoluminescence lifetime imaging configurations in a scanning electron microscope." Ultramicroscopy 197 (2019): 28-38.

[28] Kashida, S., and Y. Kobayashi. "Neutron Scattering Study of the Structural Phase Transitions in TIGaSe~ 2." JOURNAL-KOREAN PHYSICAL SOCIETY 32 (1998): S40-S43.

[29] Gasanly, N. M. "Effect of isomorphic atom substitution on the lattice parameters and the optical absorption edge of TlGaSe 2-TlInSe 2 mixed crystals." Journal of the Korean Physical Societ*y*48.5 (2006): 914-918.

[30] O.Madelung, semiconductors: data handbook. (springer Science and Business Media, New York, (2012)).

[31] Kilday, D. G., et al. "Electronic structure of the ‘‘chain’’chalcogenide TlInSe 2. " Physical Review *B* 35.2 (1987): 660.

[32] Li, Bin, Lisheng Chi, and John D. Corbett. "Na6TlSb4: Synthesis, Structure, and Bonding. An Electron-Rich Salt with a Chain Conformation and a Tl− Tl Bond Length Determined by the Cation." Inorganic chemistry 42.9 (2003): 3036-3042.

[33] Kashuba, A. I., et al. "Specific Features of Content Dependences for Energy Gap in In x Tl 1-x I Solid State Crystalline Alloys." Acta Physica Polonica, A. 133.1 (2018).

[34] Panich, A. M. "Electronic properties and phase transitions in low-dimensional semiconductors." Journal of Physics: Condensed Matter 20.29 (2008): 293202.

[35] Kanatzidis, Mercouri G., and Sandeep Dhingra. "Soluble polychalcogenide chemistry of indium. Synthesis and characterization of [In2Se21] 4-, the first indium polyselenide." Inorganic Chemistry 28.11 (1989): 2024-2026.

[36] González, L. E., and D. J. González. "Orbital free ab initio simulation of surface freezing in a dilute Ga-Tl alloy." The European Physical Journal Special Topics 196.1 (2011): 15.

[37] Hardman, Ned J., et al. "Structures, bonding, and reaction chemistry of the neutral organogallium (I) compounds (GaAr) n (n= 1 or 2)(Ar= Terphenyl or Related Ligand): an experimental investigation of Ga− Ga multiple bonding." Journal of the American Chemical Society 125.9 (2003): 2667-2679.

[38] Atuchin, V. V., et al. "Formation of inert Bi2Se3 (0001) cleaved surface." Crystal Growth & Design 11.12 (2011): 5507-5514.

[39] Filimonova, O. N., et al. "Substitution mechanisms in In, Au, and Cu-bearing sphalerites studied by X-ray absorption spectroscopy of synthetic and natural minerals." Mineralogical Magazine(2019): 1-48.

[40] Omar, A., A. F. Qasrawi, and N. M. Gasanly. "Temperature effects on the structural and optical properties of the TlInSe2xS2 (1− x) mixed crystals (x= 0.3)." Journal of Alloys and Compounds 724 (2017): 98-102

[41] Polak, Maciej P., Robert Kudrawiec, and Oleg Rubel. "Electronic band structure of nitrogen diluted Ga (PAsN): Formation of the intermediate band, direct and indirect optical transitions, localization of states." arXiv preprint arXiv:1904.00159 (2019).

[42] Hamer, Matthew J., et al. "Indirect to Direct Gap Crossover in Two-Dimensional InSe Revealed by Angle-Resolved Photoemission Spectroscopy." ACS nano (2019).

[43] Abe, Takao, Toru Takahashi, and Koun Shirai. "Mechanism for generating interstitial atoms by thermal stress during silicon crystal growth." Progress in Crystal Growth and Characterization of Materials (2019).

[44] Hu, Chun-Feng, Tong Teng, and Xin-Ping Qu. "Two-step degradation of a-InGaZnO thin film transistors under DC bias stress." Solid-State Electronics 152 (2019): 4-10.

[45] Kim, Gwang-Sik, et al. "Schottky barrier height modulation of metal–interlayer–semiconductor structure depending on contact surface orientation for multi-gate transistors." Applied Physics Letters 114.1 (2019): 012102.

[46] Jing, Huirong, et al. "Strain-engineered robust and Schottky-barrier-free contact in 2D metal–semiconductor heterostructure." Electronic Structure 1.1 (2019): 015010.

[47] Kwapil, Wolfram, et al. "Suns-ILIT: Contact-less determination of local solar cell current-voltage characteristics." Solar Energy Materials and Solar Cells 191 (2019): 71-77.

[48] Das Mahapatra, Ayon, et al. "Defect-Assisted Broad-Band Photosensitivity with High Responsivity in Au/Self-Seeded TiO2 NR/Au-Based Back-to-Back Schottky Junctions." ACS Omega4.1 (2019): 1364-1374.

[49] Brus, V. V., et al. "Graphene/semi-insulating single crystal CdTe Schottky-type heterojunction X-and γ-Ray Radiation Detectors." *Scientific reports* 9.1 (2019): 1065.

[50] Frasch, Zoltan, and Mahmoud Belaid. "Variable gain-bandwidth transimpedance amplifier." U.S. Patent Application No. 15/669,466.

[51] Sultana, Ayesha, et al. "Energy harvesting and self-powered microphone application on multifunctional inorganic-organic hybrid nanogenerator." Energy 166 (2019): 963-971.

الملخص

في هذه الرسالة تم استكشاف الخصائص الفيزيائية لبلورات $Tl_2InGaSe_4$ من خلال التحليلات البنائية، الضوئية والكهربائية. تم اكتشاف الطبيعة الطبقية لهذه البلورات باستخدام تقنية المسح الضوئي المجهري لاستخدامها في تكنولوجيا النانو. إن تحليل الأشعة السينية المعتمدة على الحرارة في المدى 300-470 K بيّن أن البلورات تتشكل من تركيبة أحادية الميلان وتركيبة رباعية الزوايا في آن واحد و أن البلورات تميل إلى تركيبة أحادية الميلان عند التسخين الحراري. و قد تبين بأن حجم الحبيبات والإجهاد الميكروي و كثافة العيوب وأخطاء التراص هي حساسة جداً للتغييرات البنائية المعتمدة على الحرارة. و بالتطابق تبين من الدراسات الضوئية المعتمدة على الحرارة أن فراغات الطاقة الضوئية تقل بشكل خطي (مباشر) مع نقصان الحرارة. بالإضافة إلى ذلك، تبين من دراسات فرق الجهد والتيار المعتمة والمضيئة أن البلورات تمتلك حساسية فائقة للضوء ولا يعتمد ارتفاع حواجز الطاقة على الاشعاع الضوئي. وعلاوةً على ذلك، تبين من تحليل طيف الممانعة في المدى 10-1800 MHz أنه يمكن التحكم في المواسعة بشكل مميز مما يؤهل البلورة للاستخدام في صناعة المكثفات القابلة للمعايرة.